Design, Development and Characterization of an Integrated Multispectral Polarimetric Sensor System

by

Dong-Hyun C. Kim

Submitted to the Department of Electrical Engineering and Computer Science
in partial fulfillment of the requirements for the degree of

Doctor of Philosophy in Computer Science and Electrical Engineering

at the

MASSACHUSETTS INSTITUTE OF TECHNOLOGY

May 2001

©MMI Massachusetts Institute of Technology
All rights reserved.

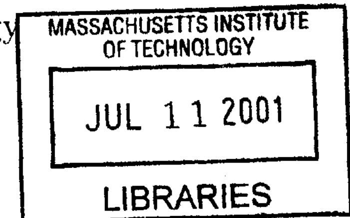

Author ....
Department of Electrical Engineering and Computer Science
May 18, 2001

Certified by.... ....
Cardinal Warde
Professor, Department of Electrical Engineering and Computer Science
Thesis Supervisor

Accepted by ....
Arthur C. Smith
Chairman, Department Committee on Graduate Students

Design, Development and Characterization of an Integrated Multispectral Polarimetric Sensor System

by

Dong-Hyun C. Kim

Submitted to the Department of Electrical Engineering and Computer Science
on May 18, 2001, in partial fulfillment of the
requirements for the degree of
Doctor of Philosophy in Computer Science and Electrical Engineering

Abstract

In this thesis, a new type of integrated imaging sensor is introduced to detect multispectral and polarimetric signatures in an infrared scene. The sensor is a stack consisting of an infrared detector array, and an array of multispectral and polarimetric filters. In this first phase of the research, a single-pixel sensor was built. Multispectral filters were initially fabricated for the 3-5 micron waveband on sapphire substrates and polarimetric filters on silicon substrates. These were characterized separately and in mechanical contact as a single unit. The transmission characteristics of both filters show excellent agreement with the theoretical results. When the filters are integrated into an imaging sensor, such a sensor is anticipated to improve image contrast with sensor-fusion post processing. In addition, it will offer portability and robustness because of its integrated nature.

Thesis Supervisor: Cardinal Warde
Title: Professor, Department of Electrical Engineering and Computer Science

Acknowledgments

This project was made possible thanks to the collective support of a large number of people.
The author wishes to thank Ken Vaccaro at the Air Force Research Laboratory for his helpful comments and direction, Charles Woods for his frequent discussion, and Alvin Drehman for the use of his sputtering machine. Thanks also to Professor Mark Schattenburg at Space Research Lab for his generosity with a grating simulation software packet and Professor Clif Fonstad and Professor David Staelin for their insightful input at the committee meetings.

The author is specially grateful to Professor Cardinal Warde for his continuous support and valuable guidance as an advisor to this project and wishes the best luck to Dave Dunmeyer who will continue and evolve this project.

Warm cheers to many friends who have made the life at MIT bearable: Yu-chul, Taejung, Junbeom, Chanhyeong, Gwangpyo, Jekwan, Joonsang, Yukyoung, Yoonkyu, et. al.

Special thanks to my family, Eunji and my parents for their eternal love and patience. Thanks to my Father for his persistence and passion, who recently published 11 books and started Ph.D. study, and to my Mother for pushing me with her indefatigable desire to learn.

This research was sponsored by the Air Force Research Laboratory under contracts F19628-99-C-0052 and F19628-00-C-0002. Support from MIT Lincoln Laboratory is also gratefully acknowledged.

Contents

1 Introduction 15

1.1 Overview of Thesis 17

2 Background 19

2.1 Polarization in Nature 19

2.2 Emission Polarization vs. Reflection Polarization 20

2.3 Stokes Parameters and Mueller Matrix 21

3 Related Work 25

3.1 Multiple-polarization/multiple-band systems 25

3.1.1 Earth Observing Scanning Polarimeter (EOSP) 25

3.1.2 Polarization and Directionality of Earth Reflectances (POLDER) 26

3.1.3 Acousto-Optic Imaging Spectropolarimeter (POLARIS II) . . 27

3.1.4 Fourier-Transform IR Spectropolarimeter (FTIRSP) 28

3.1.5 Remote Minefield Detection System (REMIDS) 28

3.1.6 Imaging Multispectral Polarimeter 31

3.1.7 Prism spectrophotopolarimeter 31

3.2 Multiple-polarization/single-band systems 31

3.2.1 MWIR Polarization Sensitive Thermal Imager 31

3.2.2 Diffraction-Grating Photopolarimeter 32

3.2.3 Airborne MWIR Polarimetric Imager 33

3.2.4 Prism-based Imaging Polarimeter 34

3.2.5 Single Shot Polarimetry Using Wedged Double Wollaston . . . 36

3.2.6 Wire-grid Polarizer Arrays Patterned with Microlithography . 36

4 Integrated Multispectral Polarimetric Sensor 39

4.1 Approach 39

4.2 Multispectral Filter Design and Fabrication 41

4.2.1 Materials 41

4.2.2 Computation of the Filter Structure 42

4.2.3 Filter Fabrication 48

5 Polarization Filter Design and Fabrication 51

5.1 Model Used in the Simulation 51

5.2 Theoretical Background 52

5.3 Simulation Results 53

5.3.1 Grating material 53

5.3.2 Substrate 56

5.3.3 Grating pitches 56

5.3.4 Grating height 56

5.3.5 Duty cycle 59

5.3.6 Higher-order diffraction 59

5.3.7 Over-etch 62

5.3.8 Under-etch 62

5.3.9 Finite aperture 62

5.4 Filter Fabrication 65

6 Multispectral and Polarization Filter Characterization 67

6.1 Multispectral Filter 67

6.1.1 FTIR measurements 67

6.1.2 Measurement with a Pt-Si camera 69

6.2 Polarization Filter 75

6.2.1 Brief discussion about optical set-up: reflective or transmissive 78

6.2.2 Unpolarized FTIR measurement of Al/Nb/Ti on a Si substrate 78

6.2.3 FTIR measurements using a ZnSe wire-grid polarizer 78
6.2.4 Instrument effects in the polarization characterization 81
6.2.5 Characterization with the Pt-Si camera 81
6.3 Multispectral and Polarization Filters in Mechanical Contact 83
6.3.1 Measured results 83
6.3.2 Characterization with the Pt-Si camera 87

7 Future Directions and Concluding Remarks 91
7.1 Future Direction 91
7.1.1 Flat Transmittance Characteristic of the Polarization Filter . 91
7.1.2 Two Polarizers in Series 93
7.1.3 Hyperspectral Filter Using Non-Uniformity 93
7.1.4 Integrated Multispectral Polarization Filter 93
7.2 Concluding Remarks 97

A Program Code to Design a Multi-layer Interference Filter Based on Simulated Annealing 99
A.1 FilterOptimization.c - non-dispersive materials 99
A.2 FilterOptimization.c - dispersive materials 103
A.3 MyMath.c 108
A.4 FilterOptimization.h 109

B Material Data in Gsolver.ini 111

C Vendor Information 113

List of Figures

1-1 Integrated multispectral polarimetric sensor in an infrared camera and its desired features . . . 17

3-1 Instrument operation of the POLDER . . . 26

3-2 Basic operation of the Acousto-Optic Imaging Spectropolarimeter, POLARIS II . . . 27

3-3 Schematic diagram of the Fourier-transform IR spectropolarimeter system . . . 29

3-4 The active/passive system operation of the REMIDS . . . 30

3-5 System diagram of the polarization sensitive thermal imager . . . 32

3-6 Diffraction grating photopolarimeter . . . 33

3-7 Schematic diagram of the Airborne MWIR Polarimetric Imager . . . 34

3-8 Prisms for imaging polarimetry (a) Wollaston (b) Rochon . . . 35

3-9 Structure of the wedged double Wollaston prism . . . 37

3-10 ematic diagram of unit cell containing a 2x2 array of micropolarizers . 38

4-1 Schematic diagrams of the multispectral polarimetric sensor . . . 40

4-2 Flow chart for optimization of multispectral filters based on simulated annealing . . . 43

4-3 Optimum structure of the multilayer subfilters on GaAs . . . 45

4-4 Optimum structure of the multispectral filters calculated for sapphire substrates . . . 46

4-5 Sensitivity of the multispectral filter to thickness variation in the layers 47

5-1 Schematics of the model in the wire-grid polarizer simulation 52
5-2 Qualitative description of why Rayleigh anomaly is outstanding for TM polarization 54
5-3 (a) Above, TM transmittance of the polarizer for each material (b) Below, extinction ratio of the polarizer for each material 55
5-4 Effects of pitch for TM transmittance of the polarizer 57
5-5 Effects of grating height on TE and TM components 58
5-6 Effects of grating duty cycle for TM transmittance of the polarizer . . 60
5-7 Higher-order components of a polarizer 61
5-8 Effects of over-etch 63
5-9 Effects of under-etch 64
5-10 Processing flowchart for wire-grid polarization filter 65

6-1 Measured transmittance of Ge/SiO/Ge/SiO on a GaAs substrate . . 68
6-2 Measured transmittance of Ge/SiO/Ge on a sapphire substrate 70
6-3 Adjusted spectral characteristic of the measured Ge/SiO/Ge sample on a sapphire substrate 71
6-4 Optical set-up used to characterize a multispectral filter 72
6-5 Emission images of a blackbody object at different temperatures . . . 73
6-6 Reflection images of a blackbody object at different infrared source temperatures (I is the current to the light source.) 74
6-7 Imaging experiment of the multispectral filter based on blackbody radiation 76
6-8 Polarization characteristics of the Nicolet 860 FTIR System 77
6-9 Calculation vs. unpolarized FTIR measurement results 79
6-10 Measurement results of the three sub-stripe polarization filters using FTIR 80
6-11 Instrument effects in the polarization characterization 82
6-12 Optical set-up to characterize polarization filter samples 83

6-13 Transmission images of the polarization filter at different polarizer orientation . . . 84
6-14 Measured results using FTIR for all combinations of multispectral passbands and polarization filter orientations . . . 85
6-15 Intensity as a function of wavelength for the subpixel corresponding to horizontal polarization and $3.5 - 4.5\mu m$ waveband with source polarization angle θ . . . 86
6-16 Optical set-up for multispectral polarization filter samples . . . 87
6-17 Transmission images of multispectral and polarization filters at different source temperatures . . . 88
6-18 Transmission images of the multispectral and polarization filters in mechanical contact at different polarizer orientation . . . 89

7-1 Transmittance of the metal wire-grid grating of multiple linewidths . 92
7-2 Processing flowchart for the triple-decker spectral polarizer plate on a common substrate . . . 94
7-3 Processing flowchart to integrate the triple-decker spectral polarizer to a sensor on a single substrate . . . 95

Chapter 1

Introduction

A sensor is a device used to sense or measure physical phenomena. Sensors detect electrical, mechanical, optical, chemical, tactile, and acoustic signatures, for example, from background, and they extract and provide the basic information about objects. Objects that may be difficult to discriminate using a single sensor are often differentiated with a multiple sensor system that exploits several signature generation phenomena to gather data about the scene of interest. The application of multiple sensors (and the fusion of their data) offers numerous potential performance benefits over traditional single sensor approaches. Employing multiple sensors, which respond to different signatures, increases the probability that an object signature will be found against a given set such as weather, clutter, or background. Multiple sensor systems, in other words, diminish ambiguity and uncertainty in the measured information by reducing the set of hypotheses about the object or event. Multiple sensors may also be used to reduce the vulnerability to false conclusions drawn from single-sensor data. For instance, missiles may carry multiple sensors to better guarantee a hit or a radar can use multiple sensors to counter-jam incoming missiles.

The goal of the research carried out in this thesis is to develop and explore the feasibility of an integrated sensor (with no moving parts) that can record the multispectral and polarization signatures of infrared scenes, so that one can subsequently achieve improved image contrast from the measured information.

For man-made objects embedded in natural scenes, multispectral signatures of

the object could depend on the surface coating of the object and/or chemical composition of man-made materials. Moreover, multispectral data are significantly less sensitive to viewing geometry and surface smoothness than are polarization data. On the other hand, polarimetric measurement takes advantage of the fact that natural backgrounds show generally little or weak polarization signatures, while man-made objects tend to radiate with polarization component[1]. A recent study for the $3-5\mu m$ waveband demonstrates that the polarized signatures of many natural objects were measured less than 0.2%, compared to 2-4% degree-of-polarization for man-made ground objects[2, 3]. In addition, polarization data often contain information about the surface orientation and/or surface properties of objects, and a polarization signal can exist even when no intensity contrast is present[4, 5]. Consequently, it is believed that polarization and multispectral imaging data are complementary. By combining the two, better contrast can thus be achieved, since they depend on different optical characteristics of the object. However, it is not clear yet what combinations of polarization and spectral measurements are optimal for object discrimination in a given scenario, for so little data have been taken in natural and man-made scenes.

This study explores the integrated nature of multiple sensor fusion by designing and building a smart-pixel sensor. This sensor integrates optical components that can determine spectral content, polarization state and intensity level in each pixel. One can use the integrated sensor in an infrared camera as shown in Figure 1-1 and then post-process the multiple outputs of each pixel with a neural-network based sensor fusion processor to perform object discrimination. This approach is anticipated to permit highly selective discrimination among objects with nearly identical spatial and spectral features, along with the compactness, portability, ruggedness and signal processing strengths achieved through the use of semiconductor integrated circuit technology. Note some desired features of the integrated sensor in Figure 1-1.

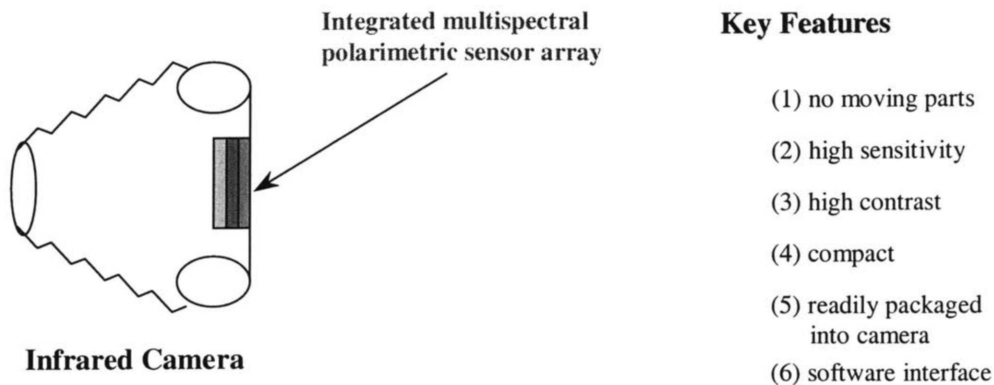

Figure 1-1: Integrated multispectral polarimetric sensor in an infrared camera and its desired features

1.1 Overview of Thesis

The next chapter describes background information to understand the environment where the proposed sensor system is to be used. This is followed by the chapter that recapitulates various multispectral polarimetric filtering strategies that have been attempted in the past. Subsequent chapters begin with a presentation of a new approach to tackle this problem, and discuss issues related to the design, fabrication, and characterization of the proposed multispectral polarimetric sensor device. Finally, the improvements and future directions are described with concluding remarks.

Appendices include the custom-made source code to design an optimum multispectral interference filter. Also included are some material parameters for the simulation of wire-grid polarization filters. Vendor information who supplied essential parts for this project is shown in Appendix C.

Chapter 2

Background

This chapter describes some basic facts about the polarization of light scattered from natural objects such as vegetation, terrain, lakes and rivers, and briefly discuss emission and reflection polarizations. In addition, this chapter also discusses man-made objects made of natural materials and the polarization characteristics of such objects.

2.1 Polarization in Nature

As was stated in Chapter 1, polarized light exists in nature. Two most well-known examples are light scattered by the air molecules in the blue sky and light reflected off water. The overhead blue sky is strongly polarized at 90°, from the sun, with its degree of polarization reaching a maximum value of about 75% at twilight. When the sky is clouded, the light is linearly polarized with its orientation determined by the illumination[6]. Cloud particles directly lit by the sun or the moon, acting as a reflecting surface, polarizes light tangentially, as in the case of the blue sky. The degree of polarization, however, may differ depending on the particle characteristics, such as composition, density and size. On the other hand, still water acts as a large reflecting surface. The reflected light is 100% linearly polarized at the Brewster angle of about 37°, to the surface.

Much part of the polarization that is observed in nature is linear polarization, oftentimes, with a reduced degree of polarization. The polarization phenomena in

nature need to be analyzed to be isolated, when the polarization sensor is to be used against the sky or the water, such as ocean or lakes.

Not all polarizing objects are linear polarizers. Some materials such as birefringent polymers and, most notably, nucleic acids convert unpolarized light into circularly polarized light upon reflection. This is due to the helical structure of the molecules the metals are composed of. Therefore, when linearly polarized light is incident, only one form of circularly polarized light is reflected. This phenomenon is called *circular dichroism*[7], which may potentially pose a problem for an incomplete sensor that discriminates only linear polarization. However, the polarization that can be found in nature is dominantly linear polarization. For example, it was reported that in the case of water surface, the contribution of the circular polarization component to the total intensity is two orders of magnitude less than that of the linear polarization component[8]. Thus, the needs to detect circular or elliptical polarization may be marginal.

2.2 Emission Polarization vs. Reflection Polarization

Polarization characteristics of an emissive object is very different from that of a reflective object. Light, reflected by a smooth surface, is polarized tangentially. Its degree of polarization becomes maximal, when the light is reflected at Brewster angle. On the other hand, the emitted light, after refracted by and transmitted through a surface, is polarized vertically, assuming that the direction of the emission is statistically random with its irradiance governed by the $cos^4\theta$ law and that there is no oxide layer which destroys polarization[9]. In addition, the emitted radiation is never polarized as much as may be possible in reflection. For this reason, it would be very tricky to exactly tell the polarization characteristics of an object in a hot daylight environment, unless the data of the object are well analyzed *a priori* at a given temperature and geometry.

2.3 Stokes Parameters and Mueller Matrix

Stokes parameters are a four-parameter representation of the state of polarization of light. For a quasi-monochromatic plane wave, they are the four quantities defined as

$$\begin{aligned} S_0 &= <a_1^2> + <a_2^2>, \\ S_1 &= <a_1^2> - <a_2^2>, \\ S_2 &= 2<a_1 a_2 cos\delta>, \\ S_3 &= 2<a_1 a_2 sin\delta>, \end{aligned} \tag{2.1}$$

where a_1 and a_2 are the instantaneous amplitudes of the two orthogonal components E_x and E_y of the electric vector and δ is their phase difference. In order to see how Stokes parameters can be useful to characterize the polarization state of light, consider a quasi-monochromatic light with a frequency f propagating in the z-direction. This can be expressed as

$$\begin{aligned} E_x(t) &= a_1(t)e^{i[\phi_1(t)-2\pi ft]}, \\ E_y(t) &= a_2(t)e^{i[\phi_2(t)-2\pi ft]}. \end{aligned} \tag{2.2}$$

Since the electric vector that makes an angle θ relative to the positive x axis is

$$E(t) = E_x cos\theta + E_y e^{i\alpha} sin\theta, \tag{2.3}$$

where α is the retardation of the y-component with respect to the x-component. Therefore, the observed intensity of the light, when transmitted through a polarizer with the appropriate orientation, is

$$\begin{aligned} I &= <E(t)E^*(t)> \\ &= <E_x E_x^*> cos^2\theta + <E_y E_y^*> sin^2\theta \\ &+ <E_x E_y^*> e^{-i\alpha} cos\theta sin\theta + <E_x^* E_y> e^{i\alpha} cos\theta sin\theta. \end{aligned} \tag{2.4}$$

Using Equation 2.2 and Equation 2.4,

$$\begin{aligned} I &= < a_1^2 > cos^2\theta + < a_2^2 > sin^2\theta \\ &+ < a_1 a_2 e^{i(\phi_1 - \phi_2)} > e^{-i\alpha} cos\theta sin\theta + < a_1 a_2 e^{-i(\phi_1-\phi_2)} > e^{i\alpha} cos\theta sin\theta. \end{aligned} \quad (2.5)$$

Since the retardation is ignored for incomplete sensor systems which measure linear polarization only,

$$\begin{aligned} I &= < a_1^2 > cos^2\theta + < a_2^2 > sin^2\theta + < a_1 a_2 cos(\phi_1 - \phi_2) > sin(2\theta) \\ &= < a_1^2 > cos^2\theta + < a_2^2 > sin^2\theta + < a_1 a_2 cos\delta > sin(2\theta), \end{aligned} \quad (2.6)$$

where $\delta = \phi_1 - \phi_2$. From Equation 2.1 and Equation 2.6,

$$\begin{aligned} S_0 &= I(\theta = 0^o) + I(\theta = 90^o), \\ S_1 &= I(\theta = 0^o) - I(\theta = 90^o), \\ S_2 &= I(\theta = 45^o) - I(\theta = 135^o). \end{aligned} \quad (2.7)$$

S_3 cannot be directly obtained for incomplete systems. For a quasi-monochromatic plane wave, however,

$$S_0^2 \simeq S_1^2 + S_2^2 + S_3^2, \quad (2.8)$$

which can be used to indirectly obtain S_3. In general, S_3 represents the amount of circularly polarized light and is usually very small. For incomplete systems, this parameter may be ignored. Note that from Equation 2.6,

$$I(\theta = 135^o) = I(\theta = 45^o) - [I(\theta = 0^o) + I(\theta = 90^o)]. \quad (2.9)$$

This means that only three independent intensity measurements of a polarizer with an orientation at 0°, 45° and 90° are necessary to characterize the state of polarization of the incident light. In terms of the Stokes parameters, the degree of polarization of light is defined as the ratio of intensity of polarized light component to total light

intensity. In other words, the degree of polarization

$$
\begin{aligned}
P &= I_{polarized}/I_{total} \\
&= \sqrt{S_1^2 + S_2^2 + S_3^2}/S_0,
\end{aligned} \tag{2.10}
$$

expressed in %. The degree of polarization is a good measure of the light polarization. For example, 0 or 100% of the degree of polarization indicates that the light is unpolarized or perfectly polarized, respectively.

While Stokes parameters are used to understand the polarization characteristics of incident light, the Mueller matrix is a 4x4 matrix representation of an optical component, which completely describes how the component affects the polarization of the partially polarized incident light. The Stokes parameters after light is sent through an optical component can be calculated by multiplying the input Stokes vector, a column vector the Stokes parameters are grouped into, with the Mueller matrix of the component. Some of the most useful Mueller matrices are collected in [10].

Chapter 3

Related Work

There have been continuing efforts to build multispectral and/or polarimetric sensors for a variety of applications in astronomy and Earth sciences. Recently, such sensor systems have been seriously developed for remote sensing and military applications. Some of the previous approaches to multispectral and/or polarimetric sensors are reviewed in what follows.

3.1 Multiple-polarization/multiple-band systems

3.1.1 Earth Observing Scanning Polarimeter (EOSP)

The EOSP[11, 12, 13, 14] is an instrument, developed for Earth Observing System (EOS) space mission platforms at NASA in late 1980s and early 1990s, to provide global mapping with multispectral photopolarimetry. Even though the EOSP was not launched as of 2000, this would allow more pronounced aerosol signature in the polarization of the scattered light, compared to the radiance. The EOSP scans a continuous sweep of the instantaneous field of view (IFOV) of the scene. The scanned scene is supplied to eight boresighted telescope and aft optics assemblies simultaneously, each of which angularly separates the incident scene flux into two orthogonally-polarized beams. Each beam is then spectrally separated into three spectral bands using dichroic beamsplitters and bandpass filters. The spectral band of the system

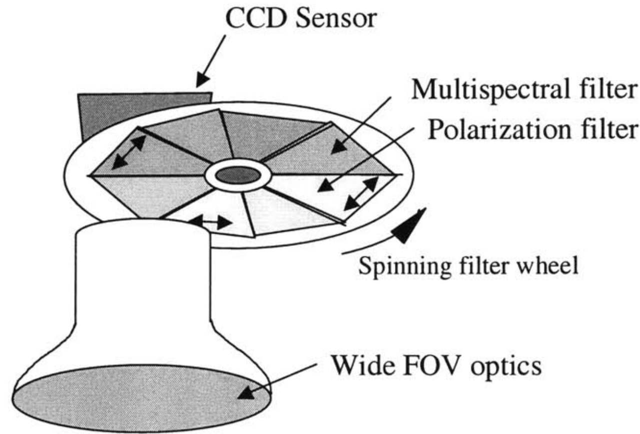

Figure 3-1: Instrument operation of the POLDER

thus covers 12 discrete passbands, ranging from 410nm to 2250nm.

3.1.2 Polarization and Directionality of Earth Reflectances (POLDER)

The POLDER[15] is an optical imaging radiometer, developed at CNES (Centre National d'Etudes Spatiales) of France and installed on the satellite of the Japanese ADEOS mission in 1995. It scans a wide field of view (50°) with moderate spatial resolution ($6 \times 6\, km^2$) and observes bidirectional reflectance and polarization distribution of the scanned scene on a global scale by taking, for a given object, measurements in variable viewing configurations along the track of the satellite. The radiation from the scene is time-multiplexed by the fast-spinning spectral filters in nine spectral bands of the visible - near infrared spectrum. Polarization states are measured at three of the nine wavelengths. The instrument is schematically described in Figure 3-1.

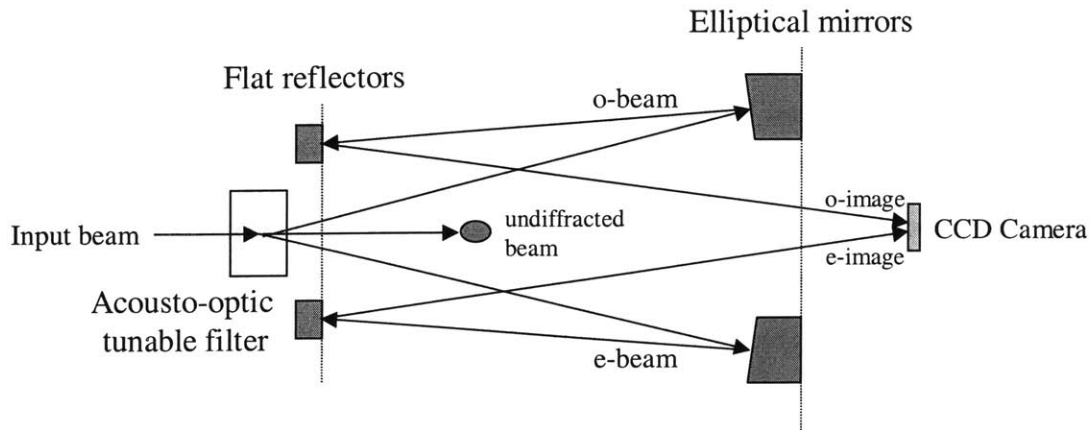

Figure 3-2: Basic operation of the Acousto-Optic Imaging Spectropolarimeter, POLARIS II

3.1.3 Acousto-Optic Imaging Spectropolarimeter (POLARIS II)

POLARIS II[16] is an imaging spectropolarimeter for ground-based astronomy, based on acousto-optic tunable filter(AOTF), constructed at NASA/GSFC(Goddard Space Flight Center) in 1989. The key component of the system is the AOTF crystal which diffracts an incoming light into different directions according to the wavelength and the polarization state of the light, when the acoustic wave propagates through the crystal. When the incoming beam leaves the AOTF, the beam becomes diffracted with $+1$ and -1 orders, polarized orthogonally to each other. These o-beam and e-beam are imaged onto different parts of a CCD camera. The basic operation of POLARIS II is shown in Figure 3-2. The system is limited by the material properties of an AOTF. Also, the wavelength tuning range is fundamentally restricted up to near infrared and only two linear polarization components are allowed by the AOTF crystal.

3.1.4 Fourier-Transform IR Spectropolarimeter (FTIRSP)

The FTIRSP measures the infrared Mueller matrix spectrum in transmission or reflection at 45° from a sample under test[17, 18]. The schematic diagram of the system is shown in Figure 3-3, where Michelson interferometer provides a sample beam of selected wavelength out of global IR source by fine-tuning the position of a mirror. The whole spectrum thus covers $2.5 - 14\mu$m. The polarization generator, composed of an achromatic retarder and a wire-grid polarizer, then polarizes the incident monochromatic light along the desired polarization direction. After the beam is scattered by the sample, its polarization state is analyzed by the polarization analyzer. The Mueller matrix of the sample for specific wavelength and incident angle(45°) can be determined from the data. Applications include testing of polarization elements such as electro-optic modulators, IR polarizers, and retarders and IR signature modeling of military target samples. A similar system to this measures 16 elements of a sample's Mueller matrix[19].

3.1.5 Remote Minefield Detection System (REMIDS)

The REMIDS[20] is a multi-channel active/passive sensor system, developed by U.S. Army since early 80s and operated on U.S. Army UH-60A Black Hawk helicopter to characterize sizes that have landmines present. Figure 3-4 shows the basic operation of the REMIDS. The system has 6 separate channels which include active laser reflectance measurements of p- and s- polarization components using Nd:YLF laser at $\lambda = 1.053\mu$m and passive thermal emission measurements for $\lambda = 8 - 12\mu$m. In the collected radiation focused by a parabolic mirror, the thermal energy is separated from captured portion of the scattered laser light by a dichroic beamsplitter. The laser light is then split into two polarization components by a beamsplitting cube. The experimental demonstration in 1990 and 1991 showed successful results, even though the results were found to be site-dependent. For example, the detection percentage exceeded 95% for surface-type landmines.

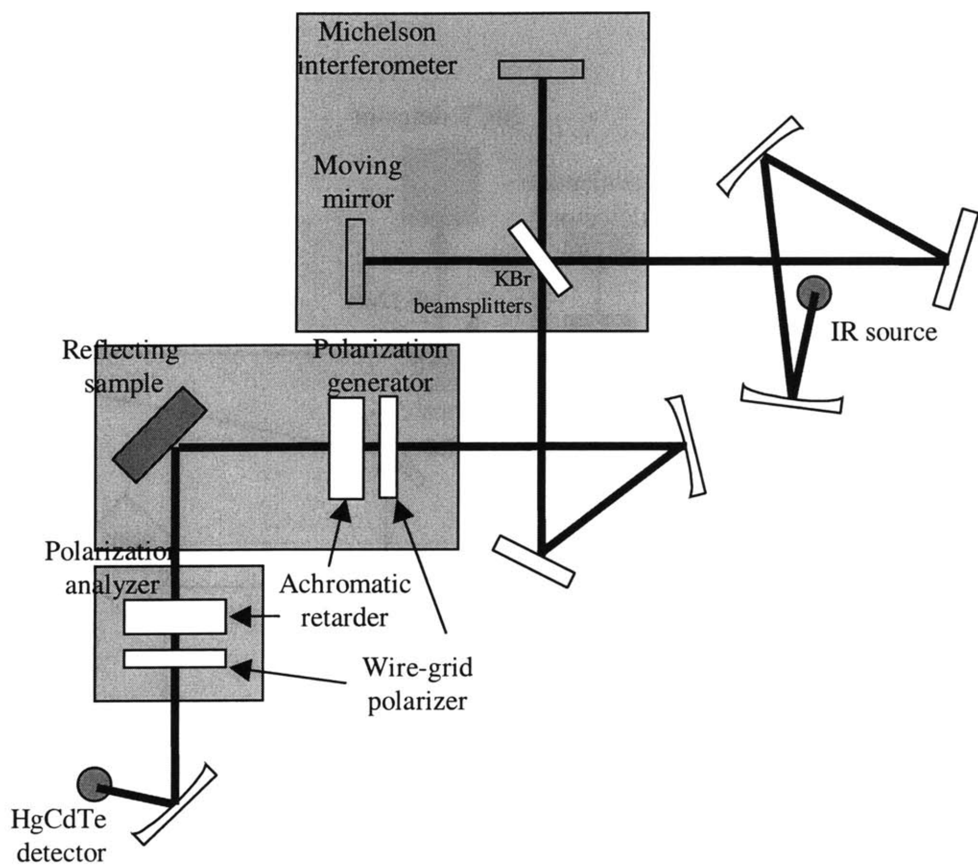

Figure 3-3: Schematic diagram of the Fourier-transform IR spectropolarimeter system

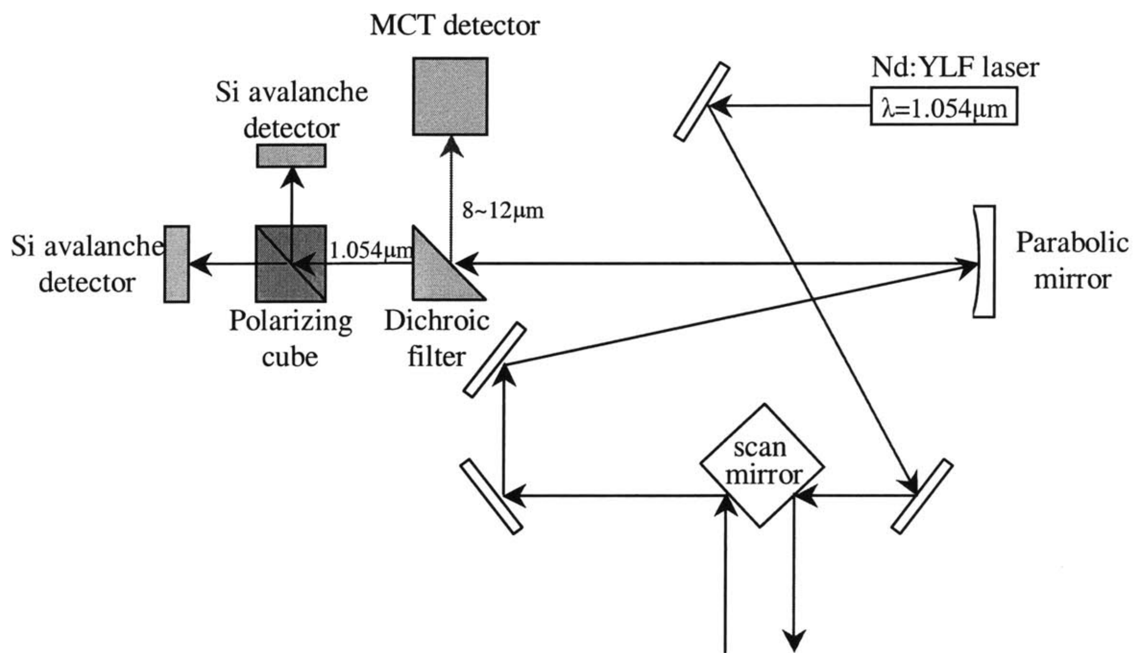

Figure 3-4: The active/passive system operation of the REMIDS

3.1.6 Imaging Multispectral Polarimeter

In this system[21], which was developed in 1998 by the Applied Technology Associates sponsored by the Air Force Research Lab, multispectral filtering is performed with a fast spinning spectral filter wheel that contains eight spectral filters. The spectral filter was created to run fast enough to produce Stokes images in a minimal time before the scene changes significantly. A complete Stokes vector of a given scene can be measured with a combination of a rotating quarter wave plate and a stationary linear polarizer in addition to the spinning spectral filter wheel. Operating range of wavelength is $0.6 - 0.85\mu m$.

3.1.7 Prism spectrophotopolarimeter

This system is an instrument to take radiometric and polarimetric measurements for astronomy, developed in 1992 by National Observatory of Japan[22]. The system is not a true spectropolarimeter in the sense that the radiometric and polarimetric measurements are not taken at the same time and the conversion between photometric and polarimetric modes is done by inserting or retracting a half-wave plate and a CaF_2 wire-grid polarizer, which takes about 5 minutes. The spectrometer employs a sapphire prism that disperses incident infrared light and refocuses it onto the 16-channel detector array. The system covers $0.9 - 2.5\mu m$ with a resolution of $0.1\mu m$.

3.2 Multiple-polarization/single-band systems

3.2.1 MWIR Polarization Sensitive Thermal Imager

The main objective of this system[23] is to take advantage of the polarization sensitivity to surface orientations for automatic object recognition. In the system, as shown in Figure 3-5, the radiation from objects, after transmitted through wire-grid polarizer array, is imaged on the thermal imaging focal plane array. The wire-grid polarizer has three angular orientations, patterned using microlithography. The wavelength range that the system covers is $3 - 5\mu m$. Few results, however, were obtained

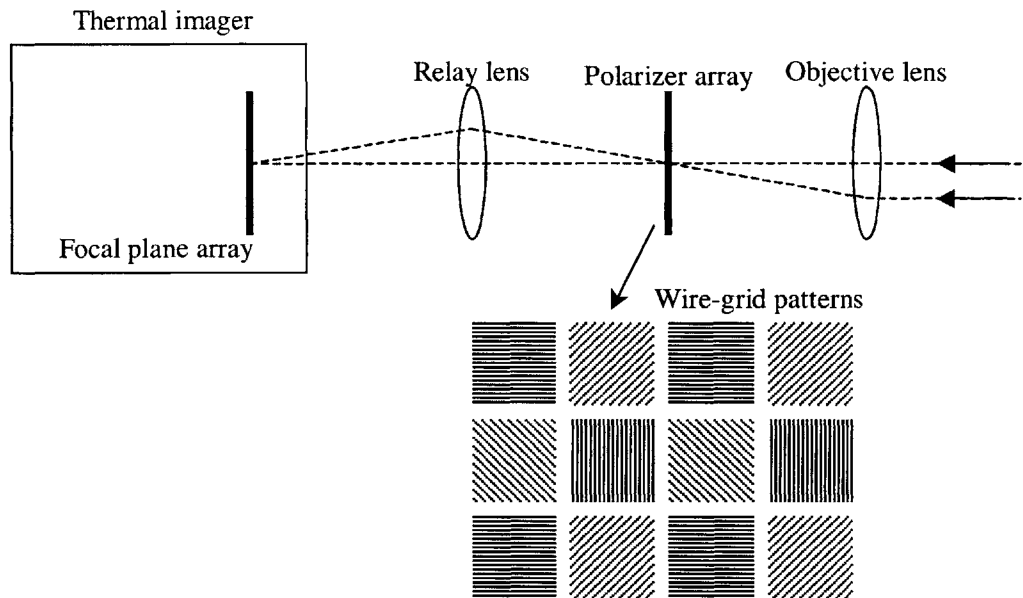

Figure 3-5: System diagram of the polarization sensitive thermal imager

experimentally.

3.2.2 Diffraction-Grating Photopolarimeter

Diffraction grating is used to make a division-of-amplitude photopolarimeter[24, 25]. This is shown in Figure 3-6. The incident light beam is diffracted by a diffraction grating and the diffracted orders are polarized by the linear polarizers in front of photodetectors at different orientations. From the detected photocurrents, four Stokes parameters are then extracted from the measured data. The dispersive nature of the system poses a significant limit on the system performance. Namely, if this system is to be applied for spectrophotometry, the system would require very high-resolution detector arrays. This is even worse for imaging spectrophotometry, which makes this

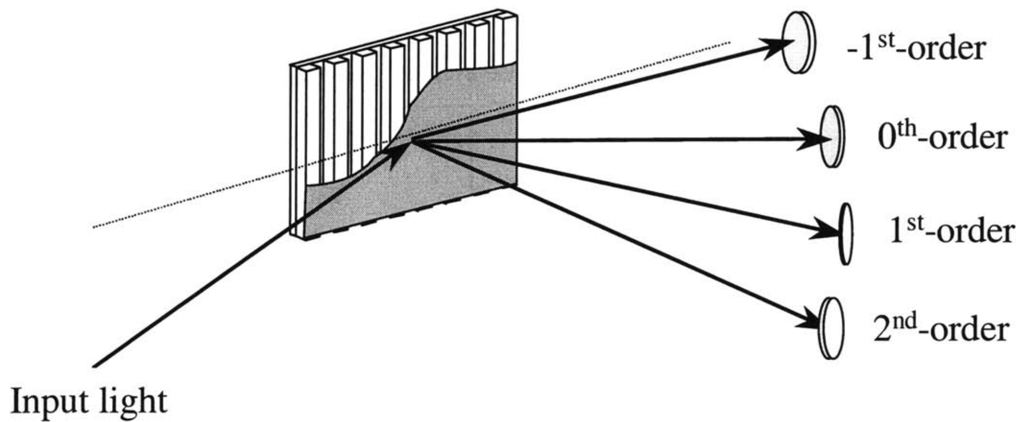

Figure 3-6: Diffraction grating photopolarimeter

system too complicated for practical purposes.

3.2.3 Airborne MWIR Polarimetric Imager

This MWIR imager was developed at the Environmental Research Institute of Michigan (ERIM) around 1996. Figure 3-7 shows the schematic diagram of this system. The incoming scene flux is divided into two polarization components by Ge Brewster plate[26]. Each of the polarized scenes from both reflected and transmitted beams is imaged sequentially in time on the IR camera. The most critical issue of the system is the band-to-band channel misregistration, which arises due to the sequential nature of the system. If channels are not precisely registered, unpolarized spatial variations in the background can leak through and appear as polarized radiance. The system

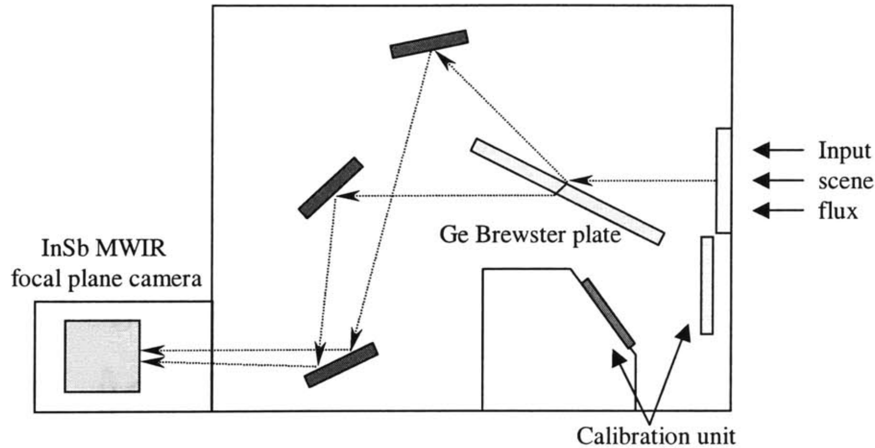

Figure 3-7: Schematic diagram of the Airborne MWIR Polarimetric Imager

operates for $4.6 - 4.9\mu m$ band at a 52Hz frame rate and has been used to collect background data ranging from rooftop, tower, fixed wing, military targets and also natural backgrounds such as vegetation and cloud.

3.2.4 Prism-based Imaging Polarimeter

This system[27] is based on a Wollaston prism or a Rochon prism to split light according to the polarization. Both Wollaston and Rochon prisms are basically a combination of two triangular prisms with optical axes at different orientations. As shown in figure 3-8, Wollaston prism allows bigger separation angle between two polarization components than Rochon prism, which makes Wollaston prism structure more advantageous for a polarimeter. While the system is relatively easy to set up using just one composite prism, it is not complete in the sense that it can tell only two polarization components. The wavelength coverage is limited by the prism, which usually covers up to near infrared.

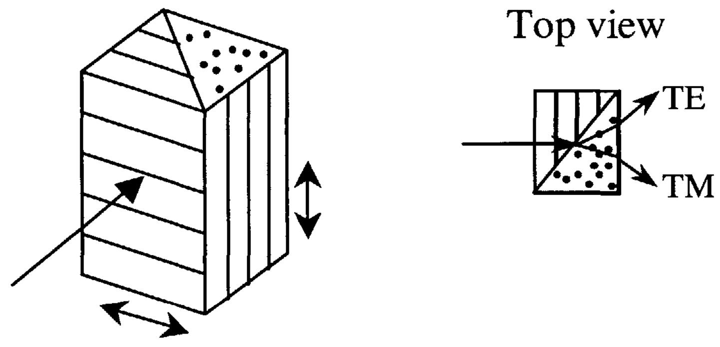

(a)

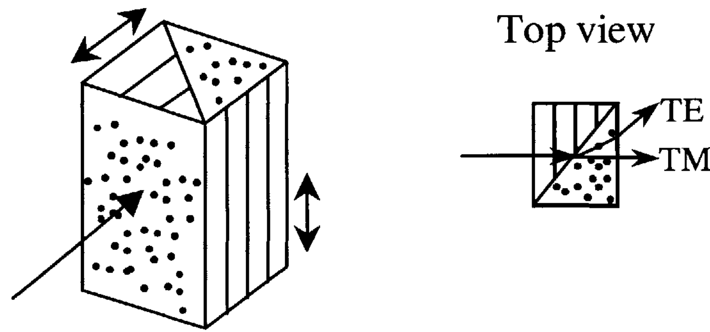

(b)

Figure 3-8: Prisms for imaging polarimetry (a) Wollaston (b) Rochon

3.2.5 Single Shot Polarimetry Using Wedged Double Wollaston

This system was first proposed in 1996 for astronomical spectropolarimetry[28]. The system is based on a combination of two Wollaston prisms and two wedges, as shown in Figure 3-9. This wedged double Wollaston prism is inserted in the pupil plane of a camera and spectrometer and the polarized flux at 0°, 45°, 90°, and 135° is simultaneously measured. The two wedges split the image and deviate all rays above and below the optical axis. The four images, after two Wollaston prisms above and below, correspond to measurements performed with polarizers at 0°, 45°, 90° and 135°. From the data, the first three elements of the Stokes vector are determined without rotating half wave plates. The prism combination was optimized for $0.3 - 2.5\mu$m.

3.2.6 Wire-grid Polarizer Arrays Patterned with Microlithography

Arrays of 256×256 micropolarizers at three angular orientations were fabricated that measure the first three Stokes vector components in each pixel of an imaging polarimeter for the $3 - 5\mu$m range[29]. Each micropolarizer consists of a 475 nm-period Mo wires in a $16\mu m \times 16\mu m$ aperture. The schematic diagram of unit cell is shown in Figure 3-10. Interference lithography is used to generate the small grating features through an etch mask layer. Even though an imaging system composed of a micropolarizer array integrated directly onto a focal plane array was assembled, and initial testing was performed, this research is still in the development phase and practically meaningful data still remain to be taken.

It is interesting to note that the majority of the previous systems do not operate in MWIR ($3 - 5\mu$m) range due mostly to the wide availability of the off-the-shelf discrete optical elements for visible and near infrared bands. None attempted to integrate polarizers with spectral filters in a compact single package with no moving parts. This may be due to the difficulty associated with the fabrication of the polarizer, in contrast to the relative facility to form a system with discrete elements.

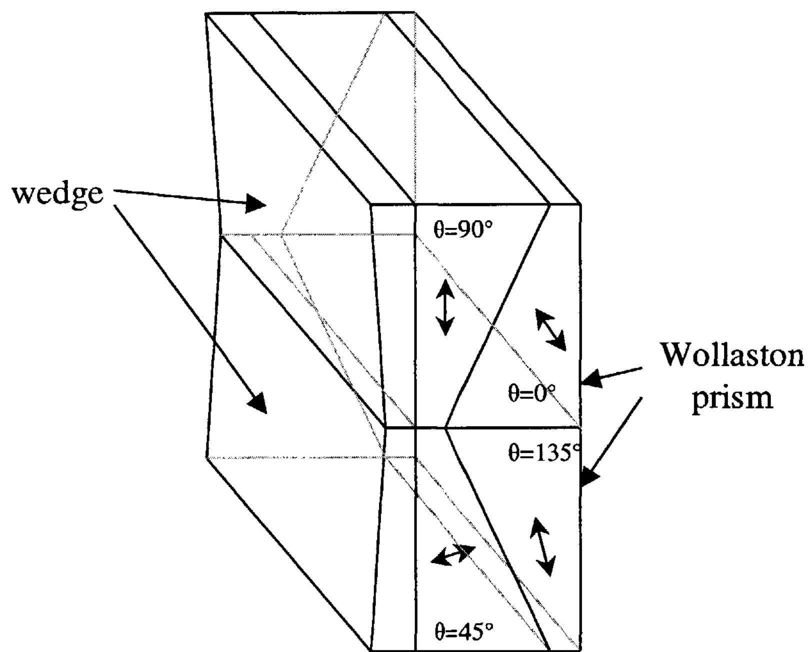

Figure 3-9: Structure of the wedged double Wollaston prism

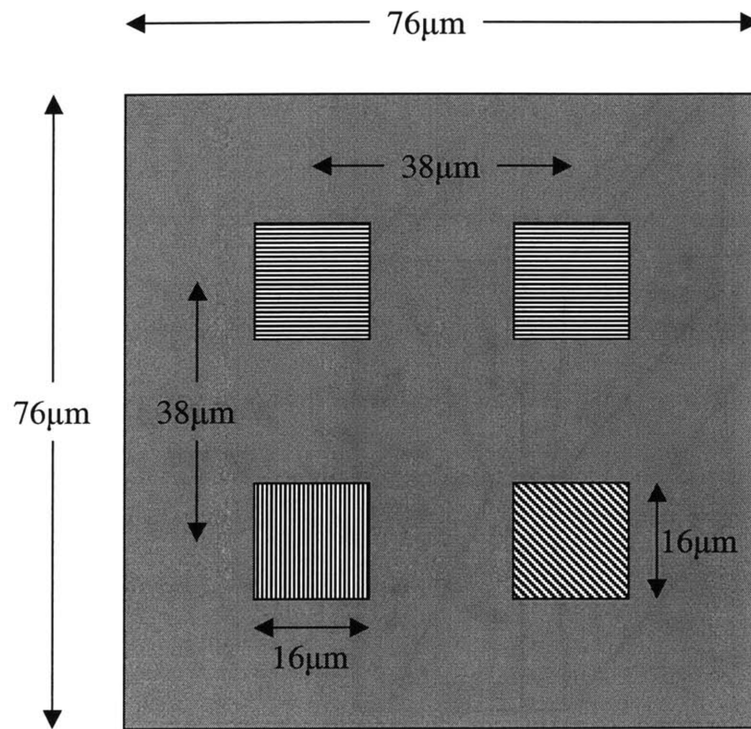

Figure 3-10: ematic diagram of unit cell containing a 2x2 array of micropolarizers

Chapter 4

Integrated Multispectral Polarimetric Sensor

4.1 Approach

The general approach of the research described in this thesis is to design and build a smart-pixel sensor which integrates optical components that can determine spectral content, polarization state and intensity level in each pixel, and which can then post-process the multiple outputs of each pixel with a neural-network based sensor fusion processor to perform object discrimination.

Figure 4-1 shows the schematic diagram of the two different structures for the sensor. The triple-decker system on the right has a multi-layer interference filter and wire-grid polarizer on top of each other, while they are laid side-by-side in the double-decker system on the left. Compared to the double-decker, the triple-decker has lower resolution and is less power-efficient. The triple-decker system, however, has the data from spectral and polarization sub-pixels perfectly registered, and moreover, it is relatively simple to fabricate due to its planar structure, lending itself to the only practical alternative for the study.

The multispectral polarimetric sensor system based on this scheme is not complete, in the sense that the system cannot distinguish circular polarized contents from unpolarized light. While it is not easy to integrate any features for circular polar-

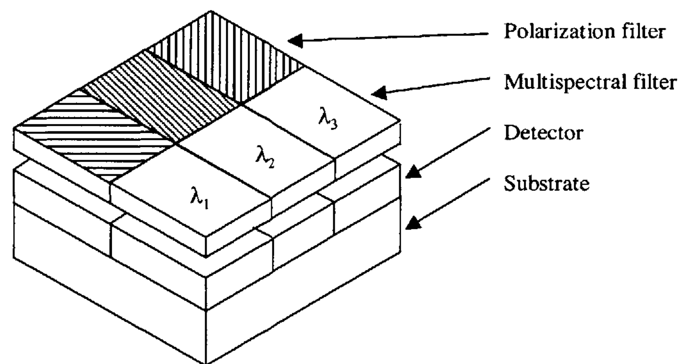

(a) Double-decker design

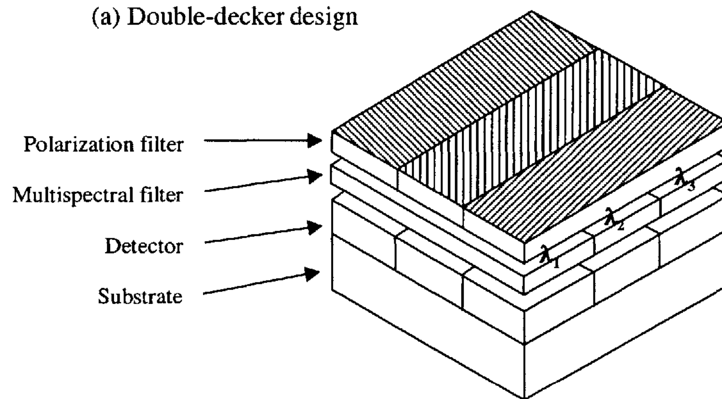

(b) Triple-decker design

Figure 4-1: Schematic diagrams of the multispectral polarimetric sensor

ization, the incompleteness may not be such an issue, since most of the natural and man-made objects polarize linearly with a few exceptions, as was briefly discussed in Chapter 2. Another potential issue with the proposed scheme in Figure 4-1 is that the spatial resolution of the system is inversely proportional to the spectral and polarimetric resolution. For this reason, it is important to estimate an optimal number for the spectral and polarimetric resolution. The system described in this thesis work has three spectral bands, equivalent to the three primary colors, and three polarization orientations, which is the minimum number required to tell linear polarization contents in an incident scene.

In the first phase of the overall program (the scope of this research), a discrete-component approach with a large pixel size was first taken to establish the operational feasibility of such a sensor concept in the $3-5\mu$m waveband. Individual components, and a spectral polarizer plate formed by sandwiching multispectral and polarization filters in mechanical contact were evaluated using a commercially available Pt-Si camera.

In the next step, the details of which are beyond the scope of this thesis, integration of multispectral and polarization filters on a common substrate will be attempted. This will be eventually followed by integration with a detector and then using sensor fusion algorithms such as the opponent processing models[30] to analyze the sensor data for object discrimination purposes.

4.2 Multispectral Filter Design and Fabrication

4.2.1 Materials

Germanium (Ge) and silicon monoxide (SiO) were used as high and low index materials of the multispectral filter, respectively. They are transparent over the wavelength range of interest and their refractive index difference is very large ($\Delta n = 2.24$ at $\lambda = 4.0\mu$m). In addition, they show good deposition characteristics on substrates such as sapphire, Si and GaAs, and are robust to the atmosphere. Ge is

widely available and is used as the high index material (refractive index $n = 4.04$ at $\lambda = 3.0\mu m$)[31, 32, 33]; it is transparent in the $2 - 15\mu m$ wavelength range. On the other hand, SiO is often used as a low-index material up to a wavelength of $7\mu m$ for infrared multi-layer filters. Its index of refraction is 1.80 at $4.0\mu m$[34]. From a processing perspective, SiO is compatible with other oxides and metals such as Si, Ge, and Al. SiO is also used as a protective over-coating for aluminum mirrors and as an anti-reflecting layer in optical applications.

The substrates on which the sensors were built are sapphire and GaAs. Sapphire is very hard and robust, and transparent in the wavelength range $0.14 - 6.5\mu m$. GaAs has advantages over sapphire in terms of photolithographic etching and processing, and availability.

4.2.2 Computation of the Filter Structure

Since general design methods[35, 36], using equivalent layers or based on Chebyshev polynomials end up with a large number of layers, three multispectral sub-filters were designed using a propagation matrix approach[37, 38], and a simulated annealing algorithm[39]. Target wavelength transmission peaks were at $3.5\mu m$, $4.0\mu m$ and $4.5\mu m$ and the half width of each band was chosen to be $0.5\mu m$ so that there was some overlap between adjacent bands. The propagation matrix corresponding to each interface between different materials is multiplied, after random numbers are assigned to each layer as thickness values. This set of thickness values is taken for the next loop, when the reflectivity calculated from the propagation matrix is closer to the desired reflectivity than in previous loop, or depending on a statistic instituted by the cooling schedule of the simulated annealing algorithm.

Figure 4-2 describes the procedure of this design process. Priority was given to the structure with the least number of layers in each sub-filter and that simultaneously had the largest number of common layers for the three sub-filters. This was done in order to simplify the fabrication process. The importance of minimal number of layers is very clear in a work[40] that attempted to implement a multispectral interference filter with 33 layers of Ge and SiO films and was plagued by a number of problems

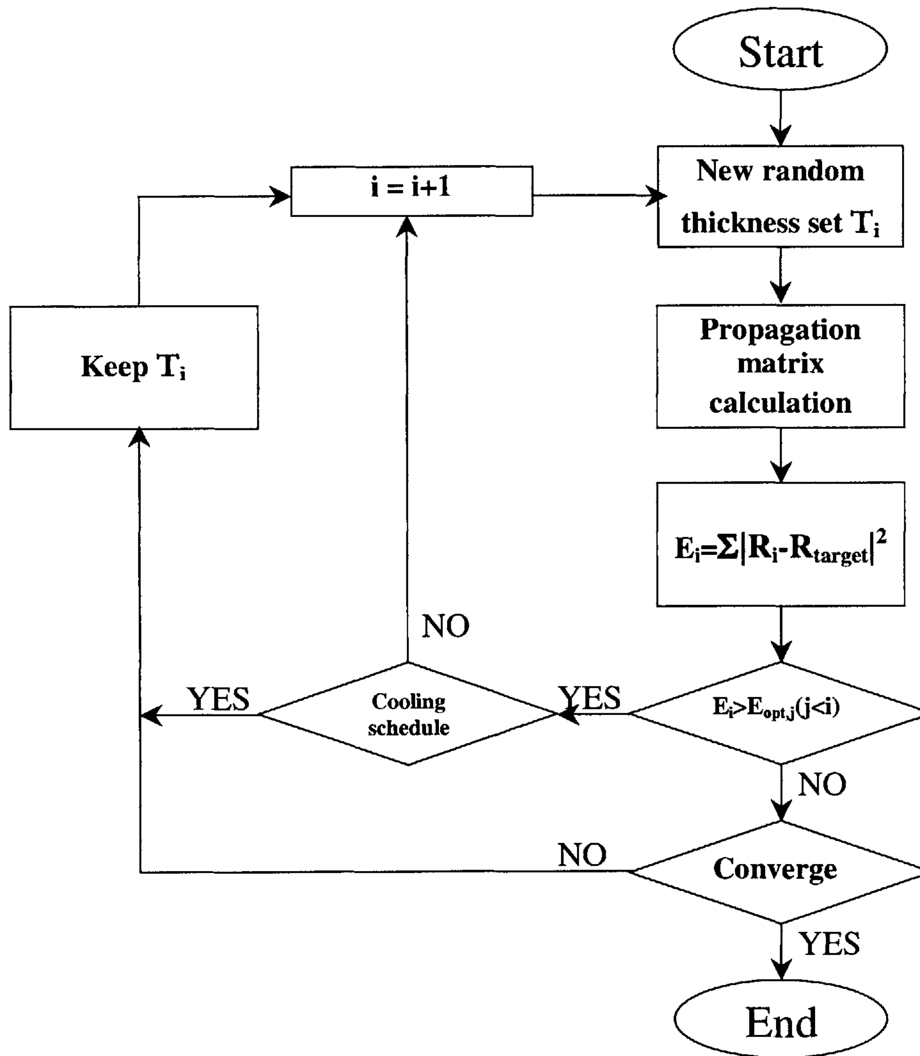

Figure 4-2: Flow chart for optimization of multispectral filters based on simulated annealing

in building a filter more than 6mm thick. Since the interference filters are optimized only for the $3 - 5\mu m$ range, it is necessary to cascade the interference sub-filters with long-pass and short-pass absorption filters to reject light outside this region. For a sapphire substrate, the substrate itself can serve as the short-pass filter since its cutoff wavelength is about $6.5\mu m$.

Figures 4-3 and 4-4 show the simulated transmittance curves for the optimum structures on GaAs and sapphire substrates, respectively. Notice that for sapphire substrates, the three-layer structure (without the first SiO layer) performs just as well as the four-layer structure. For Si or GaAs substrates, three layers never gave satisfactory results. Note that the only structured difference between the three sub-filters is the thickness of the middle SiO layer, which shifts the passband. Also note that the thickness of both Ge layers in each sub-filter is the same (2500 Å). This approach, indeed, minimizes the number of sputtering and etching step necessary to make the filters. For example, for a four-layer structure on a Si or GaAs substrate, only two sputtering runs, rather than 12, are needed to make a three sub-band multispectral filter.

The sensitivity of the sub-filter transmission characteristic to potential fabrication errors in the process of thin-film deposition is described in Figure 4-5. This figure was generated for the waveband that peaks at $4\mu m$, assuming 5% of error in some of the film thickness. A three-layer structure was assumed on a sapphire substrate for this figure. It is clear that the transmittance curve is shifted, but the general shape of the curve is conserved.

Dependence on angle of incidence and temperature

When the incident light is not perpendicular to the interference filter, there is a shift toward shorter wavelengths[41]. A collimating lens may be used to make the incident scene flux normal to the face of the multispectral interference filter. On the other hand, filter performance also depends on the operating temperature. Wavelength shifts shorter when ambient temperature is lower than the design temperature and vice versa. Usually, the wavelength shift is less than 1% for normal operating

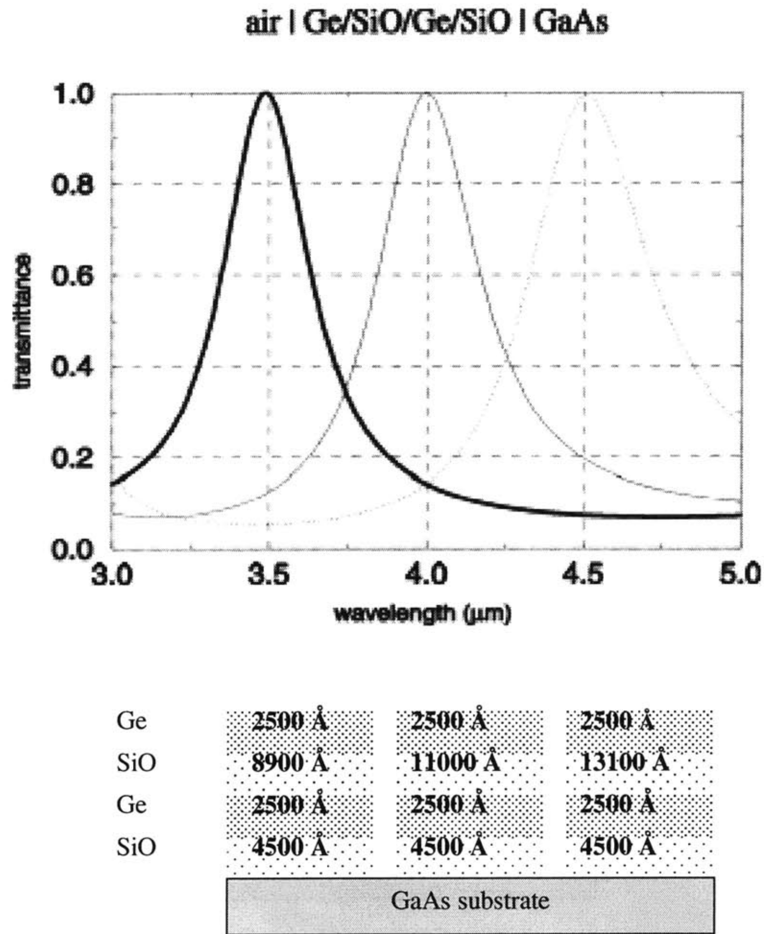

Figure 4-3: Optimum structure of the multilayer subfilters on GaAs

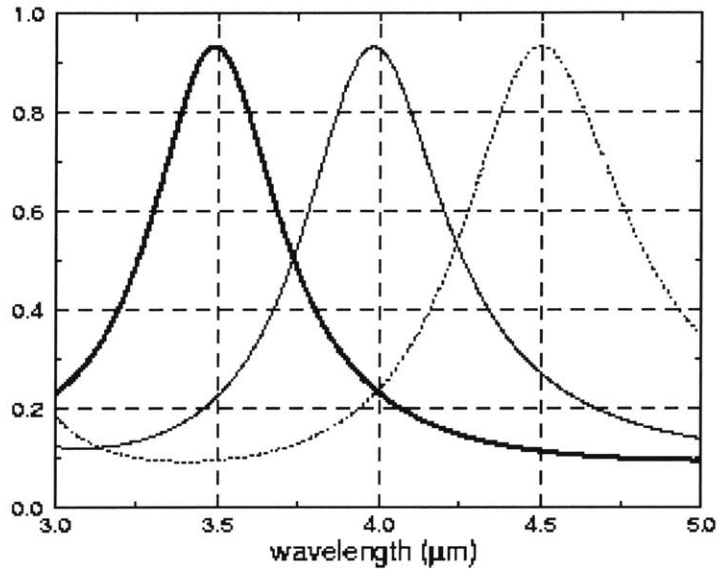

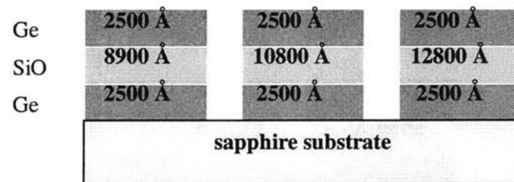

Figure 4-4: Optimum structure of the multispectral filters calculated for sapphire substrates

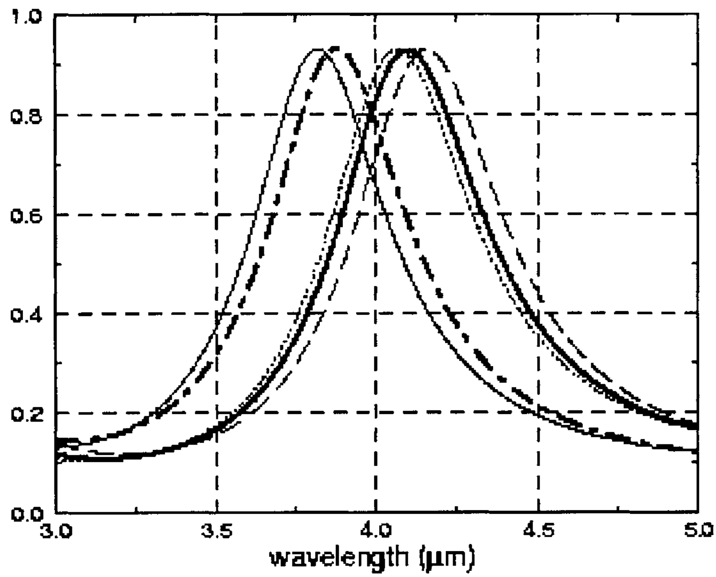

	SOLID2	SOLID1	DOT	LONG-DASHED	DOT-DASHED
Ge	0	0	-5%	0	5%
SiO	5%	-5%	5%	5%	-5%
Ge	-5%	-5%	-5%	0	0

Figure 4-5: Sensitivity of the multispectral filter to thickness variation in the layers

conditions. The temperature dependence was not considered in the design of the multispectral filter.

Effect of substrate backside

When the incident light is multiply-reflected by the backside of substrate, the reflected light will not form coarse interference fringes if the backside is not perfectly parallel to the front surface. More importantly, large thickness of a substrate, which normally ranges from $200-500\mu$m, with respect to the light wavelength makes the interference effect minimal. However, the overall transmittance of a spectral filter is reduced by the backside refraction. The computation algorithm did not consider the effect of the backside interface of substrate, which decreases the transmitted light intensity by a factor that is almost wavelength independent.

4.2.3 Filter Fabrication

In this work actual fabrication was based on the triple-decker system, because the double-decker has much more difficult processing steps than the triple-decker design. The difficulty is specifically due to the large height difference between multispectral ($\approx 2\mu$m thick) and polarization sub-filters ($\approx 0.5\mu$m thick) that are contiguous in the double-decker design.

Sapphire was selected as substrate for the multispectral interference filter, since a structure with the least number (3) of layers is available, and sapphire offers relatively high transmittance and short-pass filtering characteristic. In addition, sapphire is robust and not easily broken. To fabricate the multispectral interference filter, Ge was sputtered at 100W and SiO at 150W under 5 mtorr of Ar and 1×10^{-5} torr of base pressure. The deposition rates obtained with these parameters were 2.4Å/sec for Ge and 1.7Å/sec for SiO. It was also found that the refractive index of sputtered SiO is decreased by 10% due to the slow deposition, as was observed in previous studies[42, 43]. This is because when the deposition of SiO is carried out slowly in the presence of oxygen, the condensate acquires excess oxygen and SiO_x ($x > 1.0$)

materials are formed[44]. The refractive index of SiO thin films depends on the substrate temperature. It was reported[45] that the dependence is stronger with lower substrate temperature and that the relative refractive index difference for $3 - 5\mu$m, $\Delta n/n$, is less than 0.41%, when the substrate is at room temperature. Thin films, in general, have different properties from bulk materials. Tabulated refractive index measurements for Ge films can be found in the literature[46].

To precisely control the location of the peak transmission of each sub-filter, the middle SiO layer, which controls the peak location of the three sub-filters, was overgrown and then dry-etched with CF_4 at 50W and 10 sccm to pattern sub-filters. This dry-etching process was performed twice to define three sub-filters, each of which for $12 - 14$ minutes. The final layer thicknesses achieved were close to those illustrated in Figure 4-4.

Chapter 5

Polarization Filter Design and Fabrication

5.1 Model Used in the Simulation

From the previous studies on metal wire-grid polarizers, it has been thought that the linewidth of the wire-grid should be as small as 1/5 to 1/10 of the wavelength to obtain good polarization characteristics[47, 48, 49]. This means that the maximum linewidth required is around $0.6\mu m$ for $3 - 5\mu m$. While this is difficult to realize using conventional optical lithography, polarizers with larger pitches can still achieve sub-optimal polarization filtering characteristics with reduced polarization contrast and higher-order diffraction[47].

Figure 5-1 schematically represents the model used in the computation. Incident light is partially reflected and transmitted, each of which is diffracted by the grating. This is even more complicated by the multiple reflection inside the substrate. The wire-grid polarizer was simulated using GSOLVER 4.1[50], which is based on coupled-wave theory[51, 52].

Note that the electric field of TM polarized light oscillates orthogonally to the wires of a grating, while the TE component oscillates in parallel. In the figure, p and d denote the pitch and the thickness of the grating, respectively.

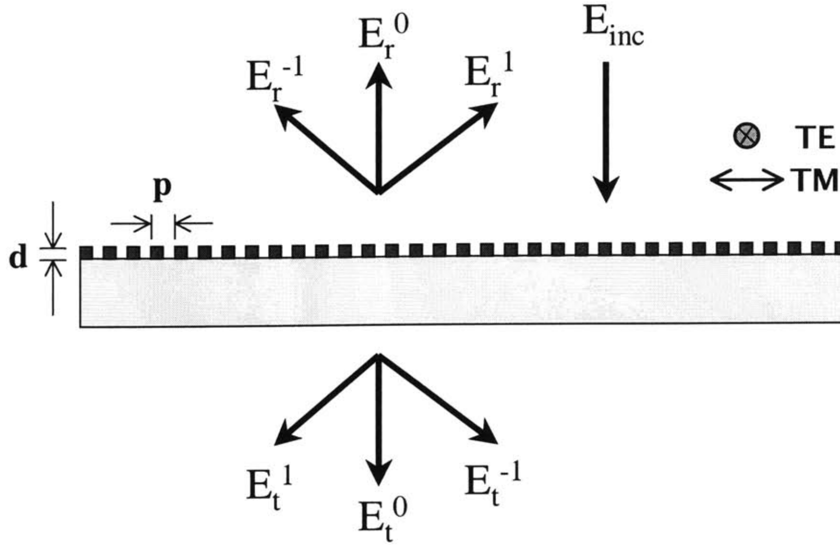

Figure 5-1: Schematics of the model in the wire-grid polarizer simulation

5.2 Theoretical Background

A grating shows a unique resonance phenomenon, which is often called 'Rayleigh anomaly'. This is due to the absorption of an incident plane wave and to the excitation of a surface wave to conserve momentum, while in the redistribution of the energy between several spectral orders at the cut-off of higher diffraction orders[53, 54]. In other words, the wire-grid polarizer will have higher-order diffracted light other than zero order, when the wavelength of the incident light is smaller than the wavelength of Rayleigh anomaly. For normal incidence, the resonance occurs when the output diffraction angle is equal to 90°. From the grating equation,

$$\begin{aligned} \sin\theta_{out,m}|_{\theta_{out,m}=90^o} &= m\lambda/p\,, \\ \sin\theta_{out,m}|_{\theta_{out,m}=90^o} &= m\lambda/n_s p. \end{aligned} \tag{5.1}$$

It is possible to calculate the grating pitch at which the anomaly occurs, where $\theta_{out,m}$ is diffraction angle for m-th order, p is the pitch of the grating and n_s is the refractive

index of the substrate. For example, the resonance wavelength for Si ($n_s = 3.43$) with 2.0μm pitch are 6.86μm, 3.43μm, 2.0μm, etc, which is confirmed theoretically and experimentally in Figures 5-4 and 6-10, respectively.

Note that the Rayleigh anomaly is prominent only for TM polarization component. For TE, the electric field is parallel to the surface of the grating. (See Figure 5-2.) On the other hand, the electric field is orthogonal to the wires of the grating for TM polarization. If the grating is a good conductor, it absorbs and does not sustain an electric vector in the surface. This makes the field strength in a TE polarization order propagating parallel to the surface much less than that of a TM order. In other words, the electric field oscillates orthogonally for the most part with respect to the grating wires, after the light is transmitted through a wire-grid grating polarizer. For a TE polarization component, less energy remains to be redistributed, when the order passes off and the anomaly is less severe[55]. An interesting point is that TE polarization shows a TM-like resonance dip, when the grating is deposited with a thin dielectric layer, since this layer does not absorb TE polarization any more[56].

5.3 Simulation Results

5.3.1 Grating material

Initially, Al, Au, and Nb were taken into consideration as a grating material in the simulation. Figure 5-3 shows the transmittance of the 0th-order TM component in (a) and the extinction ratio between TM and TE components in (b) with an assumption that each material is deposited 5000Åthick on a Si substrate with 2.0μm pitch. As shown in Figures 5-3(a) and (b), Al exhibits the best polarization contrast, while Nb grating shows comparable performance over $3 - 5\mu$m region. In fact, Nb was chosen as the grating material, due to the availability of dry-etchant gas (CF_4). For Al and Au, the grating should be based on wet etching, which is hard to control for sub-micron features.

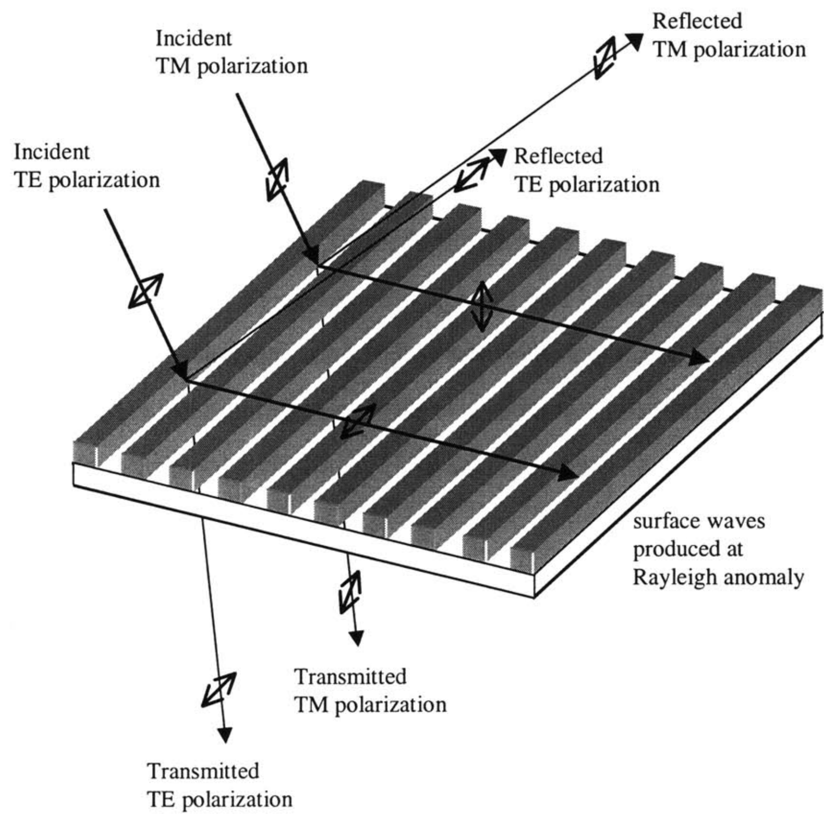

Figure 5-2: Qualitative description of why Rayleigh anomaly is outstanding for TM polarization

5.3.2 Substrate

Three substrates were available, Si, GaAs, and sapphire. Si empirically demonstrated the best contact in optical lithography, which may be directly related to the fact that the Si substrate used in experiments was very thin (200μm). Achieving good contact in lithography is critical to form sub-micron features. Sapphire was particularly unsuitable as a substrate, because this is transparent for the ultraviolet light used in optical lithography and, therefore, causes internal multiple exposure.

5.3.3 Grating pitches

Figure 5-4 shows calculated polarization characteristics of a 5000Åthick Nb grating on a Si substrate. In the figure, which represents the transmittance of the 0th-order TM component, Rayleigh anomaly is clearly observed.

Even though the wire-grid polarizer with a sub-micron pitch shows very good performance, this is very difficult to fabricate. (For example, it is typical to get an extinction ratio of more than $1,000$ with a 1.0μm pitch.) On the other hand, the wire-grid polarizer with a pitch between 1.0μm and 1.5μm suffers from a Rayleigh resonance dip in the middle of $3 - 5\mu$m wavelength range. Therefore, this is not a good choice for MWIR. Clearly, an additional important criterion is that for chosen pitch, the Rayleigh resonance falls outside the operating wavelength range. Consider a polarizer with 2.0μm pitch. From the grating equation, the primary resonance wavelengths for Si ($n_s = 3.43$) are 6.86μm and 2.0μm, which fall outside $3 - 5\mu$m wavelength range and is confirmed experimentally in Figure 23. Precise determination of the pitch is also limited by the beam address size of electron beam lithography systems.

5.3.4 Grating height

Figure 5-5 shows the effects of grating height for Nb grating of 2.0μm pitch on a Si substrate. For thicker grating, while the transmittance of the TM polarization is marginally improved, the TE polarization becomes much weaker, which leads to

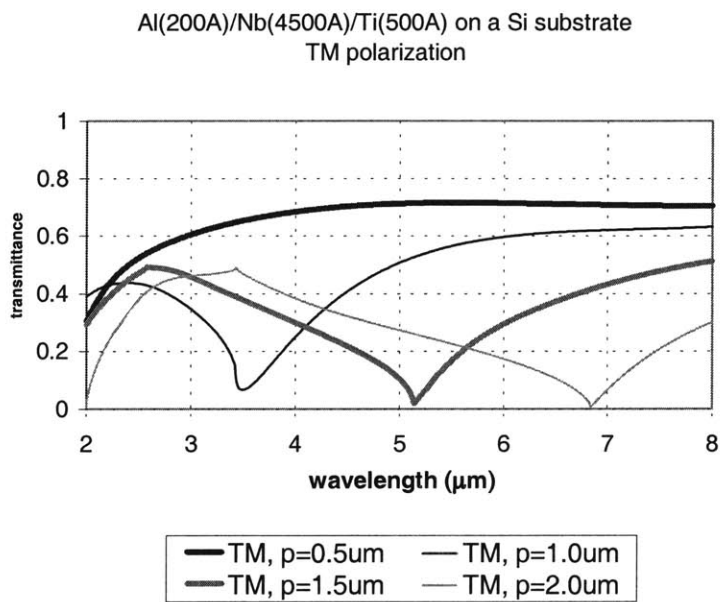

Figure 5-4: Effects of pitch for TM transmittance of the polarizer

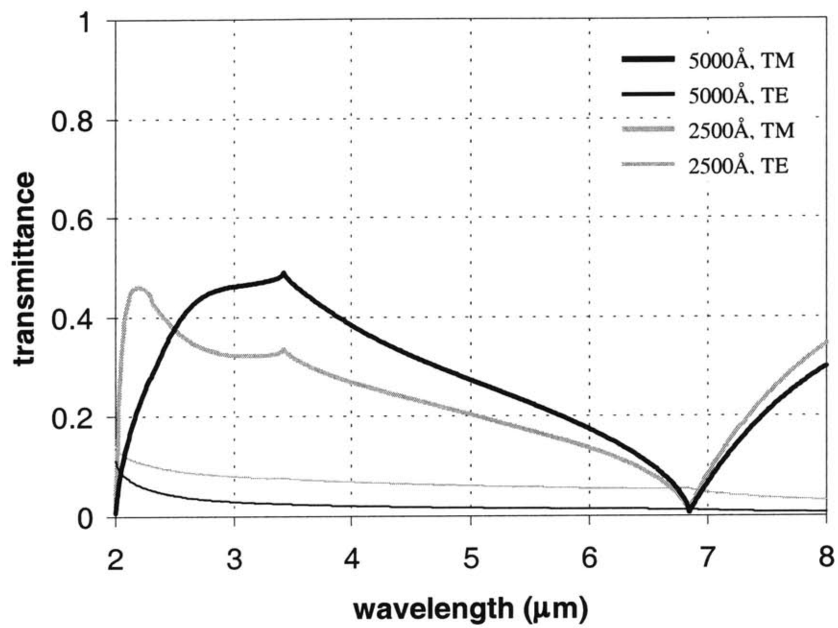

Figure 5-5: Effects of grating height on TE and TM components

larger extinction ratio.

5.3.5 Duty cycle

Even though the linewidth of a wire-grid polarizer is typically designed to be an exact half of the pitch for no apparent reason, actual linewidth is often different, smaller than a half pitch, due to the lateral etch during dry-etching step. This is illustrated in Figure 5-6. With reduced duty cycle, more light can transmit without the influence of the grating structure. Therefore, the transmittance of TM components increases considerably, especially for longer wavelength. This, however, is also accompanied by an increase of TE transmittance as well, which aggravates the polarization contrast in the $3-5\mu$m range.

5.3.6 Higher-order diffraction

Higher-order diffraction exists when the light wavelength is shorter than the longest wavelength of the Rayleigh anomaly. For example, for a wire-grid polarizer on a Si substrate ($n_s = 3.43$ at $\lambda = 4.0\mu$m) with 2.0μm pitch, the longest Rayleigh resonance wavelength is 6.86μm. Higher-order diffraction, thus, exists for the light with $\lambda <$ 6.86μm. The higher-order diffraction is undesirable, because this reduces the signal-to-noise ratio of a sensor system. The noise due to the higher-order diffraction, however, is likely to be reduced or removed using several techniques. The most obvious is using a very small pitch. According to the grating equation, a polarizer with grating pitch smaller than 0.87μm ($= 3\mu m/n_s$) does not have higher-order diffraction for $3-5\mu$m wavelength range. It may also be possible to reduce the noise, if the sensor is designed such that the active layer of the detector is very thin on the substrate surface.

Figure 5-7 shows TM and TE polarization components of the higher-order diffraction for 2.0μm pitch and 50 % duty cycle of an Al(200Å)/Nb(2500Å)/Ti(500Å) wire-grid grating on a Si substrate. The transmittance of the 0th order is 20% at $\lambda = 4.0\mu$m, while that of $\pm1^{st}$ orders is 17 %. Reflectance is about 56 % at $\lambda = 4.0\mu$m and the

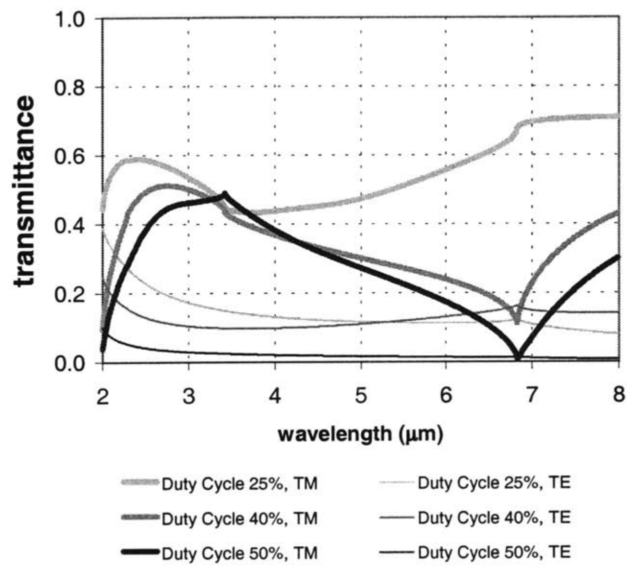

Figure 5-6: Effects of grating duty cycle for TM transmittance of the polarizer

Al(200A)/Nb(4500A)/Ti(500A) on a Si substrate

TM polarization

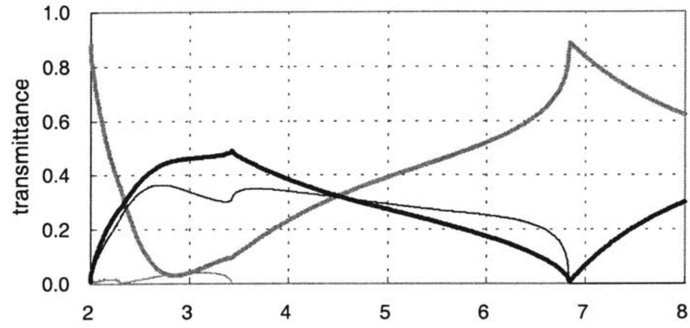

TE polarization

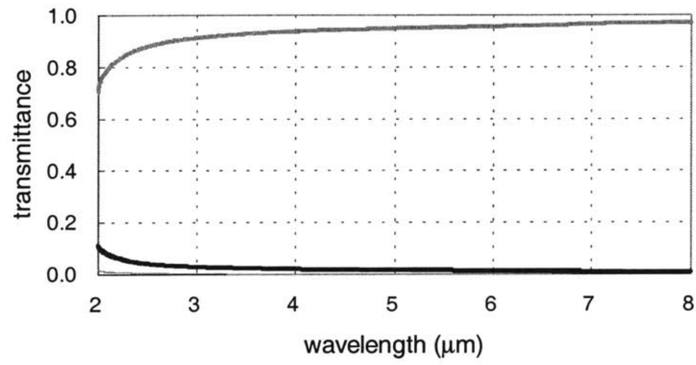

Reflection
2nd-order transmission
1st-order transmission
0th-order transmission

Figure 5-7: Higher-order components of a polarizer

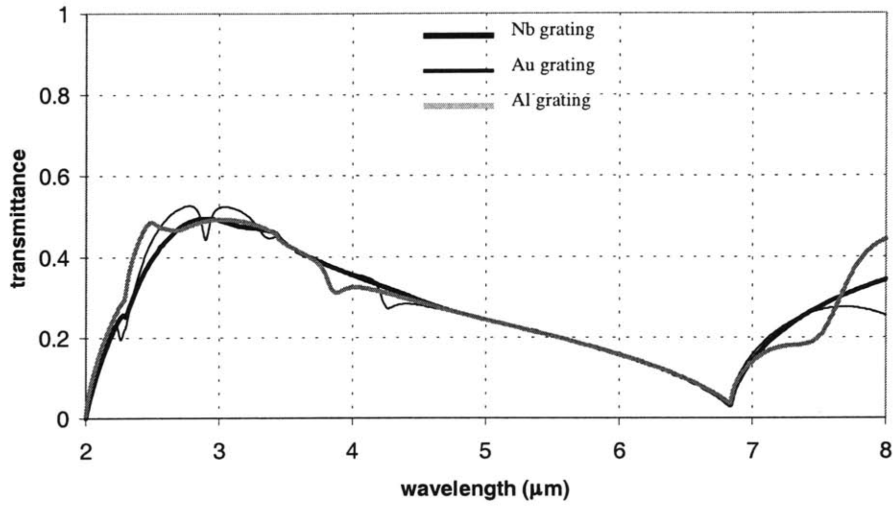

(a)

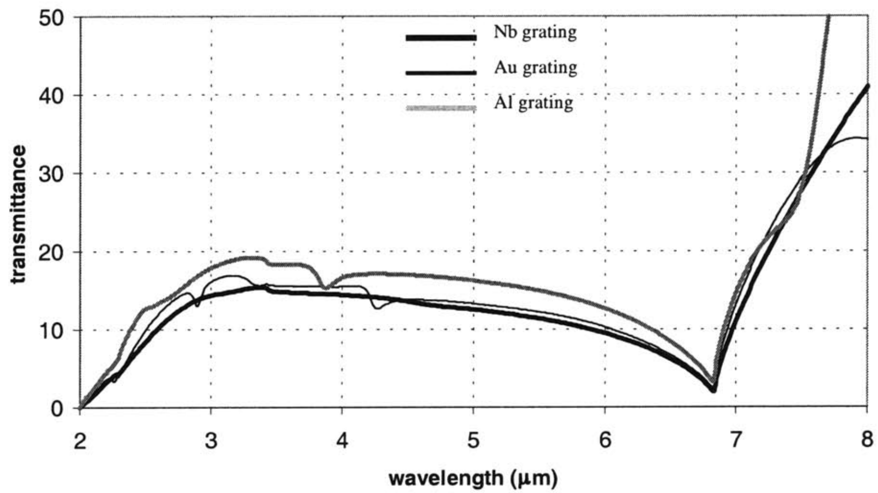

(b)

Figure 5-3: (a) Above, TM transmittance of the polarizer for each material (b) Below, extinction ratio of the polarizer for each material

rest 7% is absorbed in Nb layer. This means that only 20% of input power is available for polarization filtering.

5.3.7 Over-etch

Dry-etching with CF_4 does not stop on a Si substrate. Therefore, it is unlikely, if not impossible, to etch exactly as designed. This sub-section investigates an over-etched Al/Nb/Ti grating. Effects of under-etch are investigated in the next sub-section.

Figure 5-8 describes an over-etched Al(200Å)/Nb(4500Å)/Ti(500Å) grating with a 2.0μm pitch on a Si substrate. An over-etched grating is equivalent to a grating of Al/Nb/Ti/Si on a Si substrate. Since Si is transparent to infrared, it can be deduced that the transmittance does not change considerably with over-etching, as observed in the Figure 5-8. Part of the incident light slips through the Si layer. This reduces the extinction ratio between TM and TE components, since TE transmittance increases. The resonance is less noticeable for TM polarization.

5.3.8 Under-etch

Figure 5-9 describes an under-etched Al(200Å)/Nb(4500Å)/Ti(500Å) grating with 2.0μm pitch on a Si substrate. Incident light is absorbed by the remaining Ti film on an under-etched Al/Nb/Ti grating, which decreases transmittance and simultaneously reduces the resonance effect of a grating.

5.3.9 Finite aperture

Simulation results so far assumed infinite size of wire-grid polarizer aperture. However, actual wire-grid polarizer is of finite size. If an arrayed wire-grid polarizer with a 2.0μm pitch has a pixel size in the order of 100μm, close to that of a typical sensor element, there are only 50 wires in one pixel available for polarization. Reduced number of wires may reduce the polarization efficiency of a wire-grid polarizer. A recent study investigates the effects of the finite aperture size in more detail[57].

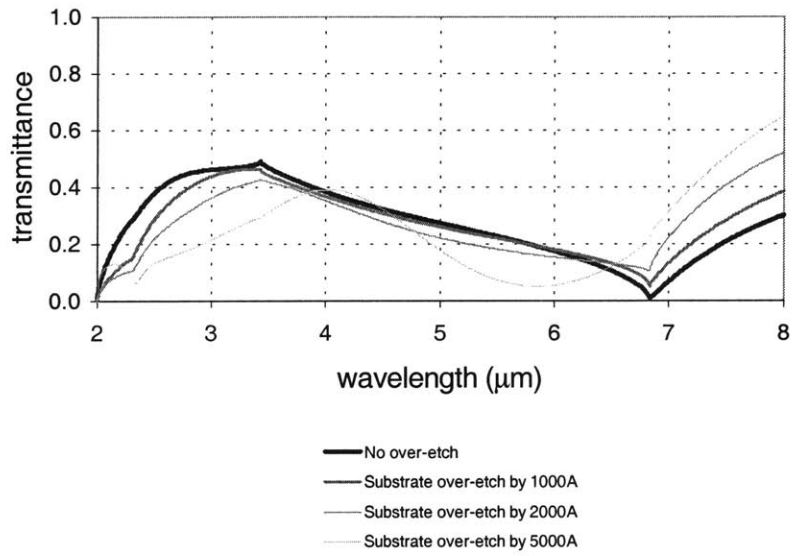

Figure 5-8: Effects of over-etch

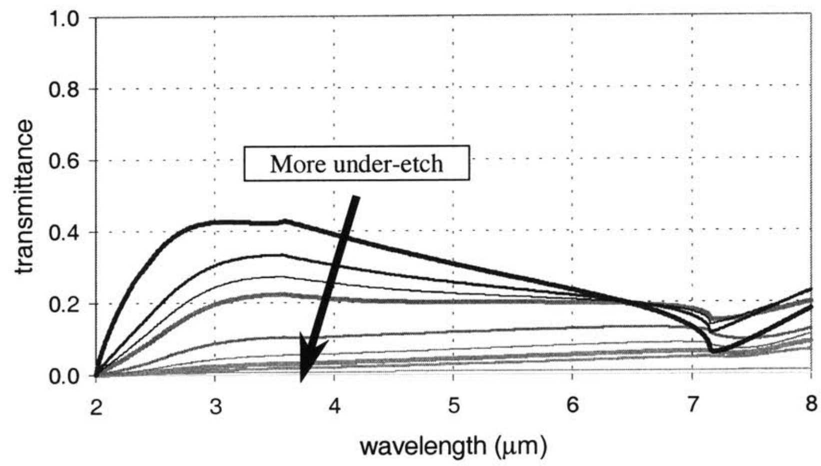

Figure 5-9: Effects of under-etch

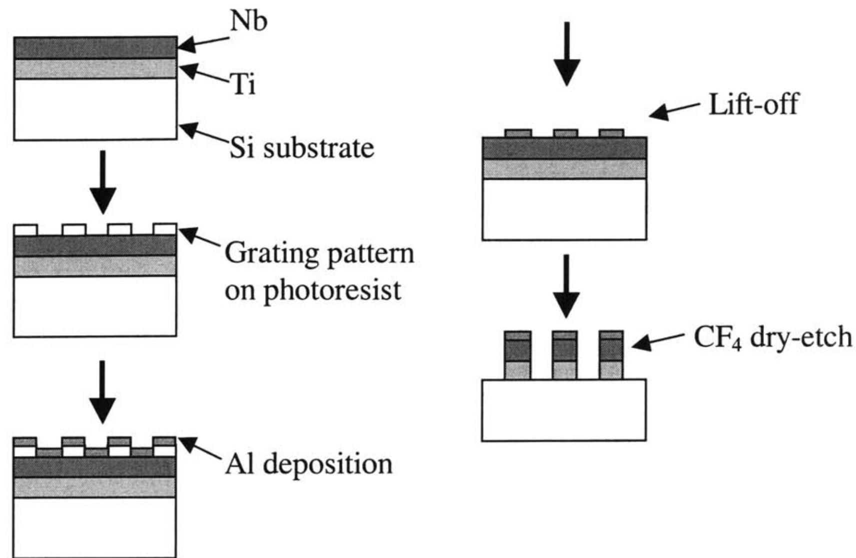

Figure 5-10: Processing flowchart for wire-grid polarization filter

5.4 Filter Fabrication

Permissable and reliable fabrication processes have been extensively searched for. Al deposition, followed by dry-etching, does not work, due to the lack of a proper dry-etchant gas available. Instead, a combination of Al, Ti, and Nb was used to fabricate the polarization filters. More specifically, Ti and Nb films were first deposited on a Si substrate. This was followed by optical lithography process. The details of the process are as follows.

1. HMDS spin coating for 45 seconds at 5000rpm

2. AZ4110 spin coating for 45 seconds at 5000rpm

3. Softbake for 30 minutes at 90°

4. Exposure for 15 seconds at $15 \mathrm{mW/cm^2}$

5. Develop for 60 seconds with 1 : 4-DI:AZ400K solution

A very thin Al layer was then evaporated on top of the patterned photoresist layer. After lift-off, only Al that is directly on Nb/Ti films remains, against which dry-etching is performed with CF_4 for $12 - 15$ minutes. This forms the final grating pattern on Al/Nb/Ti films. Figure 5-10 illustrates the fabrication process.

The fabricated polarization filters had a grating pitch of 2μm, and Nb thickness of 2000Åand 4500Å. The Al and Ti thicknesses were 200Åand 500Å, respectively, for both polarization filters.

Chapter 6

Multispectral and Polarization Filter Characterization

Characterization of multispectral and polarization filters was first performed with an FTIR. Perkin-Elmer Lambda 9 spectrometer and a Nicolet 760 spectrometer at the Air Force Research Lab at Hanscom, MA, were used for FTIR measurements for multispectral filters. For polarization filters, Nicolet 860 was used. In imaging experiments, the multispectral and polarization filters were characterized with a Prism-D Pt-Si camera of FLIR Systems Inc. Operating spectral range of Nicolet 860 system was $400 - 4000\text{cm}^{-1}$. Prism-D Pt-Si camera is equipped with two lenses made of silicon and zinc and operates for $3.6 - 5.0\mu\text{m}$.

6.1 Multispectral Filter

6.1.1 FTIR measurements

Figures 6-1 and 6-2 show the transmission characteristics of the multispectral filters on GaAs and sapphire substrates, respectively. In Figure 6-1, transmission peaks of the multispectral filter on GaAs were measured to be at $3.50\mu\text{m}$, $3.95\mu\text{m}$, and $4.48\mu\text{m}$. This filter consists of four interchanging layers of SiO and Ge, as designed in Figure 4-3. The middle SiO layer was dry-etched to tune the peak wavelength at

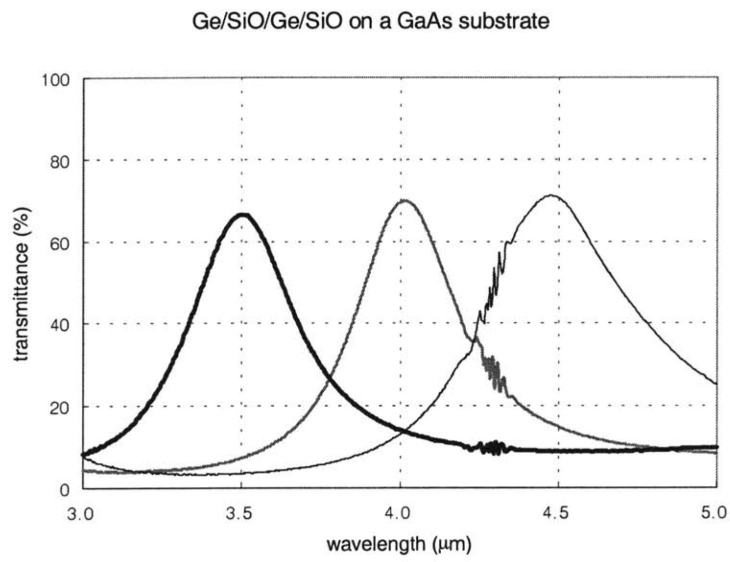

Figure 6-1: Measured transmittance of Ge/SiO/Ge/SiO on a GaAs substrate

the target. The peak transmittance was reduced to 70%, because of the refraction on the backside of the substrate. Note that sharp wiggles are present in Figure 6-1 around 4.3μm, due to the detector noise of the FTIR system.

Figure 6-2 shows the spectral characteristics of a multispectral filter on a sapphire substrate, plotted with the simulated results. Compared with the one on a Si or GaAs substrate, this filter has less deposition steps and its efficiency is enhanced with reduced backside refraction of a sapphire substrate. The power lost due to the reflection on the backside is 6.35% at $\lambda = 4.0\mu$m for sapphire substrates, while it is 27.4%, and 30.1% for GaAs and Si substrates, respectively. This reflection loss can be minimized by coating an anti-reflection film on the backside. The measured transmission peaks are located at 3.52μm, 3.99μm, and 4.44μm. The measured bandwidth of the filter is somewhat larger than simulated. This broadening is partly due to the non-uniformity of the middle SiO layer in the dry-etching process and partly because the probing beam size of FTIR is approximately 5mm, which is in the order of the pixel size of the sample. Currently, the peak shift caused by the non-uniformity is less than 0.3μm within a sub-filter. This non-uniformity is expected to improve with more precise control of dry-etching process. The influence of large probing beam size of FTIR can be adjusted with forward calculation. As a result, the effect of a neighboring sub-pixel was estimated to contribute around 7% more power. This means that about 14% of the measured power is attributed to the neighboring pixels. The adjusted spectral characteristic is shown in Figure 6-3.

6.1.2 Measurement with a Pt-Si camera

Figure 6-4 shows the optical set-up used in this experiment, where a spectral window was made for $3 - 6.5\mu$m wavelength region using a longpass filter and a sapphire substrate. The emission image of a blackbody object heated to a variable temperature is collimated by two CaF_2 lenses and then captured by the Pt-Si camera. The longpass filter was manufactured by Corion Inc. on a sapphire substrate. The passband transmittance of the longpass filter was approximately 78% for $3 - 5\mu$m wavelength range.

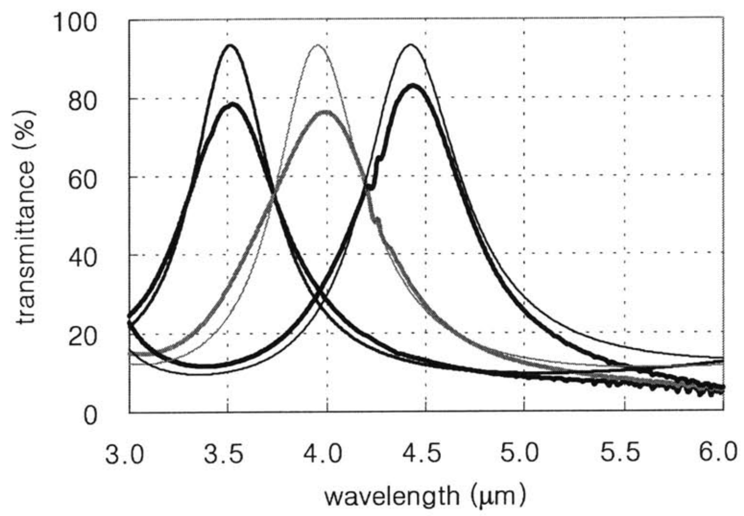

Figure 6-2: Measured transmittance of Ge/SiO/Ge on a sapphire substrate

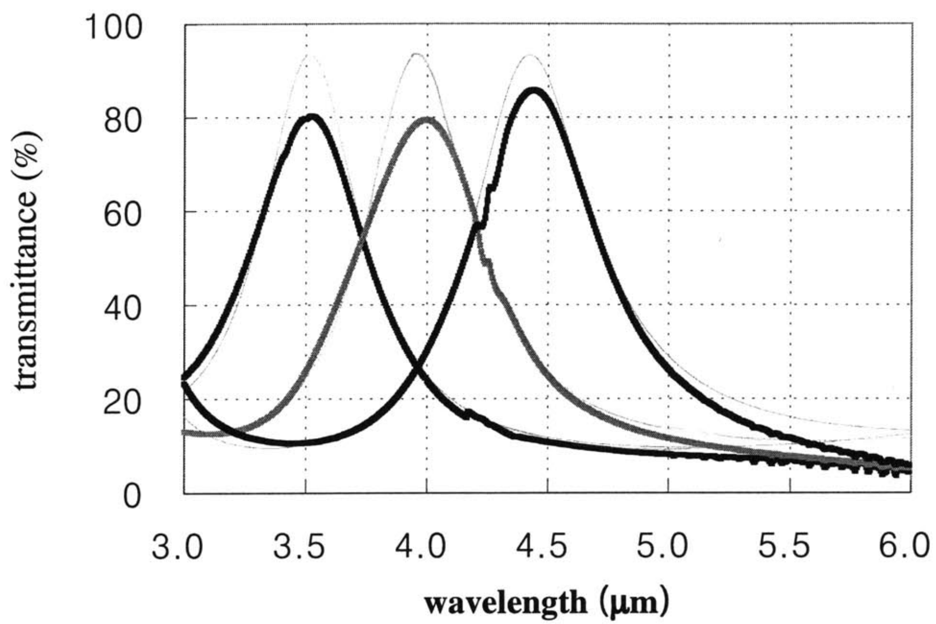

Figure 6-3: Adjusted spectral characteristic of the measured Ge/SiO/Ge sample on a sapphire substrate

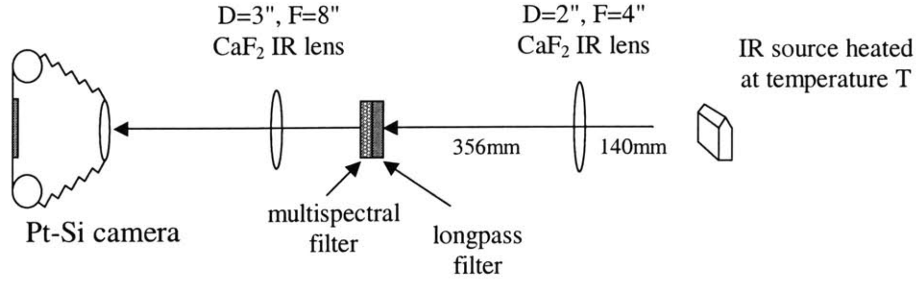

Figure 6-4: Optical set-up used to characterize a multispectral filter

Figure 6-5 shows infrared images of a metal piece, measured at different temperatures. When the object is cold, the $4 - 5\mu$m band sub-filter corresponding to the lowest energy captures the most photons. As the temperature rises, $3.5 - 4.5\mu$m and $3 - 4\mu$m sub-bands, in turn, become populated. This is illustrated in Figure 6-7. Both x and y axes of Figure 6-7 are normalized with the wavelength, λ_{max}, at which the radiance reaches maximum and the maximum radiance, w_{max}, respectively. According to Wien's displacement law for the blackbody radiation[58], λ_{max} is given as

$$\lambda_{max} = \frac{2897.8}{T\,(in K)}\ \mu m \tag{6.1}$$

and

$$W_{max} = 1.288 \times 10^{-15} T^5\ W/cm^2 \mu m. \tag{6.2}$$

The main solid curve displays the normalized blackbody radiation, while the dotted curves are the computed spectral characteristics of the multispectral filter. The overall radiance that an IR camera sees can be calculated by multiplying the multispectral filter characteristics with the blackbody radiation curve. Since the multispectral filter

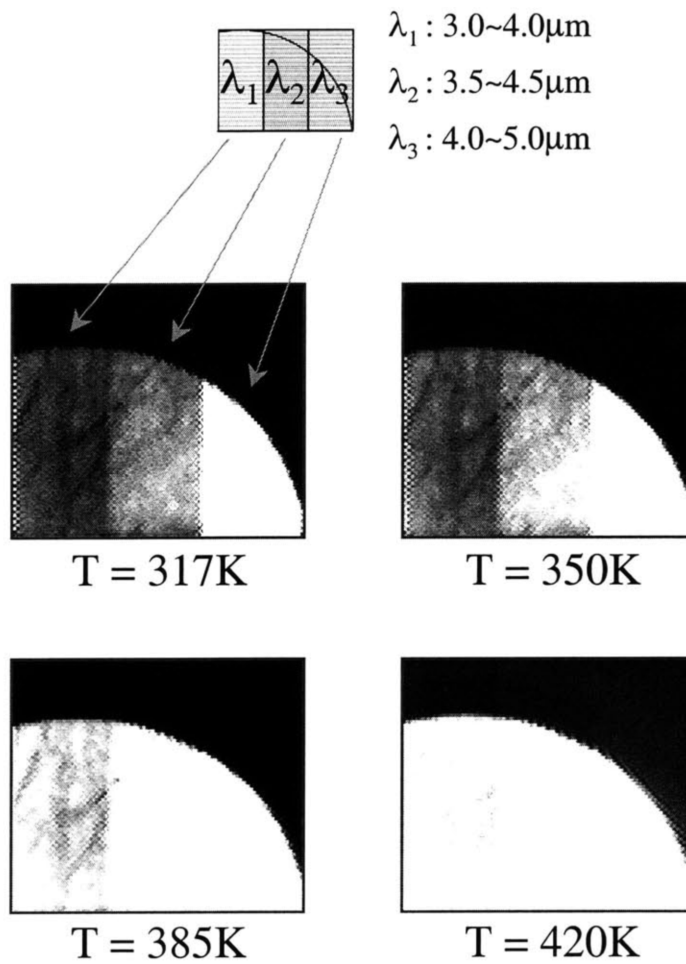

Figure 6-5: Emission images of a blackbody object at different temperatures

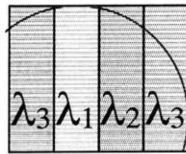

λ_1 : 3.0~4.0μm

λ_2 : 3.5~4.5μm

λ_3 : 4.0~5.0μm

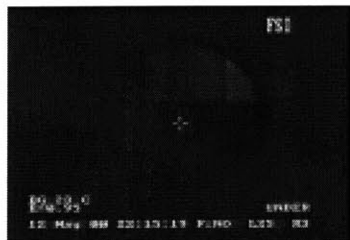

I=0.50A

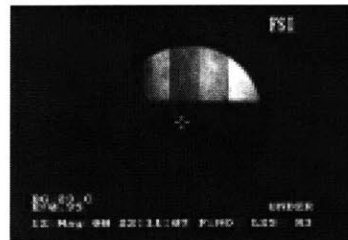

I=1.00A

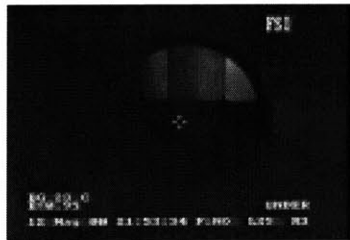

I=0.75A

I=1.25A

Figure 6-6: Reflection images of a blackbody object at different infrared source temperatures (I is the current to the light source.)

curves in Figure 6-7 are located in the left half of the blackbody radiation curve for the temperatures of interest, the longer wavelength is always brighter than the shorter wavelength at the temperature. As the temperature rises, the multispectral filter curves move toward λ_{max} and the radiance relative to w_{max} is increased to more than twice. This is clear by comparing the curves at $320K$ and $420K$ in Figure 6-7. Note that this is because λ_{max} becomes shorter with higher temperature from Wien's displacement law. When the radiance eventually reaches out of the dynamic range of the camera, the camera pixels become saturated.

The fine patterns that are observed in each sub-filter image of Figure 6-5 are associated with the rough scratchy surface of the metal piece. The light radiation varies due to the microstructures on the surface and its intensity is governed by $cos^4\theta$ law. Note that what is observed in Figure 6-5 is an emission image of object. While an emission image could make an interesting case in the polarization characterization, as discussed in Section 2.2, the multispectral filter does not discriminate and is independent of polarization. Figure 6-6, on the other hand, shows reflection images of a metal mirror, measured at different infrared source temperatures. The source temperature is controlled by the current fed to the blackbody source, I. Just as the emission images in Figure 6-5, shorter wavelength sub-bands become populated and the corresponding images become bright, as the source temperature is increased. Since the same metal piece was used as a mirror, identical patterns due to rough surface are observed in the figure.

6.2 Polarization Filter

A commercial ZnSe polarizer manufactured by Spectra Tech Inc. was employed to polarize the source in FTIR experiments and in imaging characterization using a Pt-Si camera. This polarizer is Al wire-grids of 1200 lines/mm on a ZnSe substrate and is effective for $20,000 - 500$ cm^{-1}. The polarization characteristics of the FTIR system using this polarizer were measured and described in the next sub-section.

Probe light in an optical system which is not intended for extensive polarization

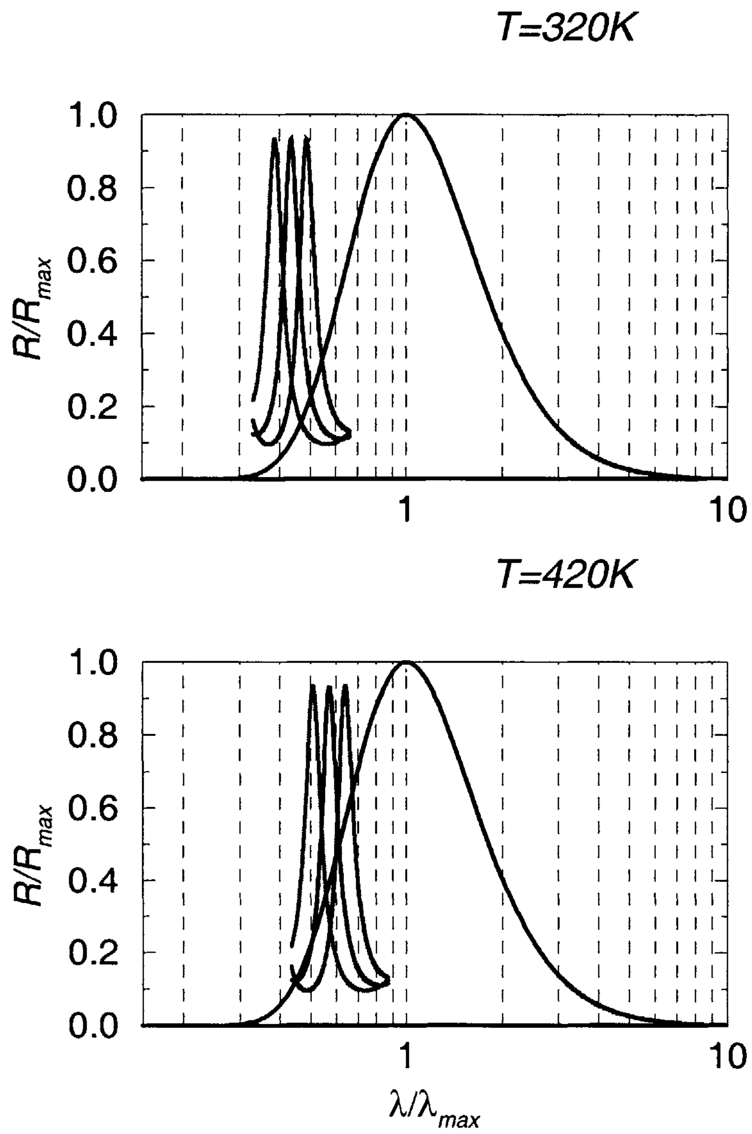

Figure 6-7: Imaging experiment of the multispectral filter based on blackbody radiation

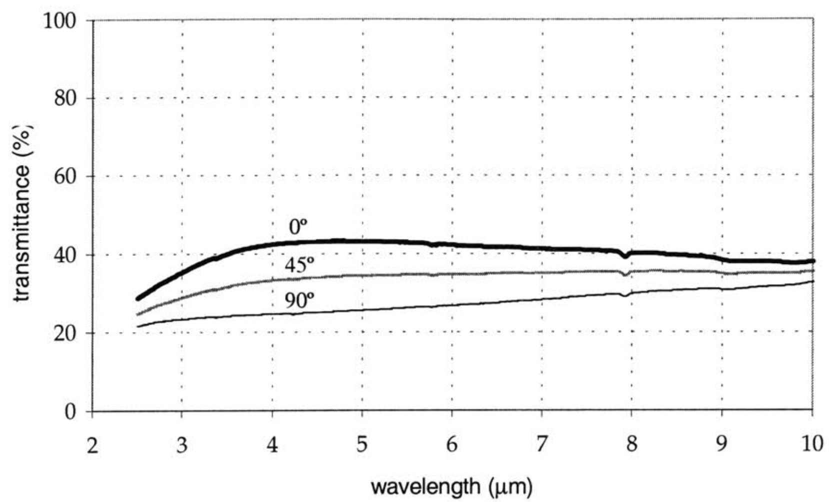

Figure 6-8: Polarization characteristics of the Nicolet 860 FTIR System

measurements such as an FTIR is often weakly polarized[59]. For example, Figure 6-8 illustrates the transmittance of the FTIR source polarized by a commercial ZnSe polarized at 0°, 45° and 90°. Here, 0° and 90° polarizations denote polarizations orthogonal and parallel to the table plane. The measured degree of polarization of the source is approximately 25% for $3 - 5\mu$m range.

6.2.1 Brief discussion about optical set-up: reflective or transmissive

Optical set-up can be designed based on either reflection or transmission at the filter. In the case of a reflection set-up, however, it should be borne in mind that additional effect of polarization exists due to the reflection by substrate. If grating vector is parallel to the TE polarization (its electric field oscillating normal to the plane of incidence), the overall polarization contrast is enhanced[60]. If it is orthogonal, on the other hand, the overall polarization contrast is diminished. Therefore, a transmissive set-up is more appropriate to remove the effect of the substrate and to achieve uniform polarization contrast.

6.2.2 Unpolarized FTIR measurement of Al/Nb/Ti on a Si substrate

Figure 6-9 shows the FTIR result when Al/Nb/Ti (200Å/2000Å/500Å) grating on a Si substrate was illuminated with an unpolarized FTIR source. The comparison with the calculation, assuming that the unpolarized source is composed of an equal portion of TE and TM components, exhibits consistency with the measurement.

6.2.3 FTIR measurements using a ZnSe wire-grid polarizer

A single-pixel multispectral filter sample on a Si substrate of Al/Nb/Ti (200Å/2000Å/500Å) grating was measured using FTIR with the source polarized by the ZnSe polarizer.

Figure 6-10 is FTIR measurements of the three polarization sub-filters, each

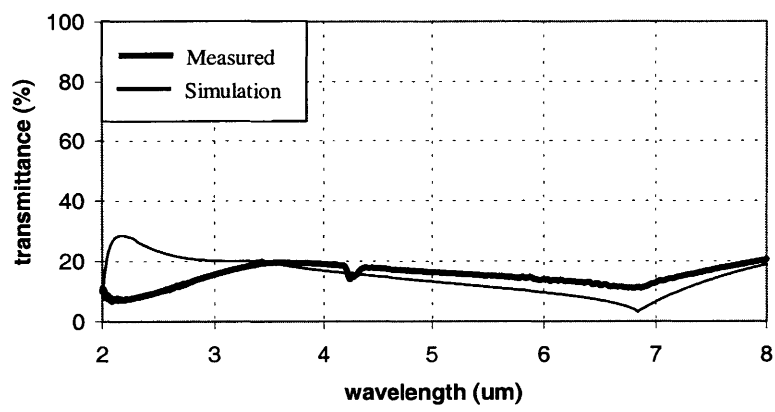

Figure 6-9: Calculation vs. unpolarized FTIR measurement results

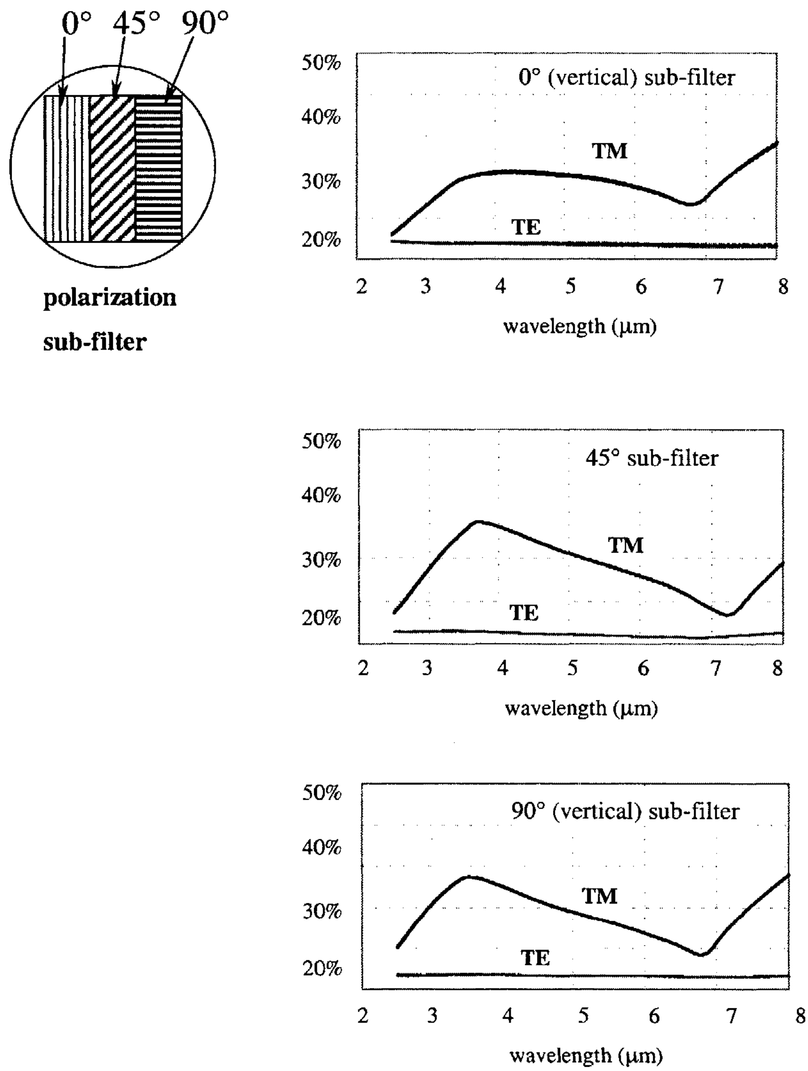

Figure 6-10: Measurement results of the three sub-stripe polarization filters using FTIR

of which corresponds to 0° (vertical), 45°, and 90° (horizontal) polarizers, respectively, after adjusting the effect of the ZnSe polarizer. Employing the Jones vector representation[61], the Jones matrix of an FTIR measurement with the ZnSe polarizer can be written as

$$\begin{pmatrix} P(TM) & 0 \\ 0 & P(TE) \end{pmatrix} \cdot \begin{pmatrix} S(TM) & 0 \\ 0 & S(TE) \end{pmatrix} \quad (6.3)$$

where P represents the Jones matrix for the ZnSe polarizer and S for the sample polarization filter. Equation 6.3 holds true when the polarization sample is in parallel with the ZnSe polarizer. For a good polarizer, $P(TE) \ll P(TM) < 1$ and $S(TE) \ll S(TM) < 1$. In order to isolate the effect of the polarization filter sample, FTIR data should be calibrated with the measured data of the ZnSe polarizer taken alone at corresponding orientation angles.

6.2.4 Instrument effects in the polarization characterization

Figure 6-11 shows an image of an instrument effect that was captured while characterizing the wire-grid polarizer with the Pt-Si camera. This is known as the narcissus spot[62] and caused by the fact that on-axis detector pixels see cold radiance of the detector that is reflected by the polarizer substrate, while off-axis pixels see warm ambient radiance. Additional instrument effects that may be observed in polarization imaging are described in the reference[63].

6.2.5 Characterization with the Pt-Si camera

Figure 6-12 shows the top-view of the optical set-up used to characterize the polarization filter samples. The rotatable ZnSe polarizer was used to polarize the infrared source vertically. In this set-up, the orientation of the polarization filter sample is fixed and only ZnSe polarizer is rotated.

Transmission images through the polarization filter are shown in Figure 6-13. Since incident light is polarized perpendicularly to the optical table by ZnSe polar-

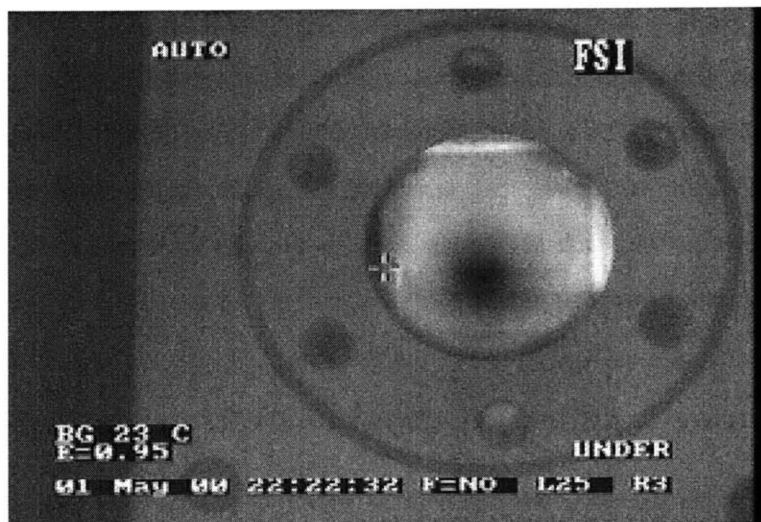

Figure 6-11: Instrument effects in the polarization characterization

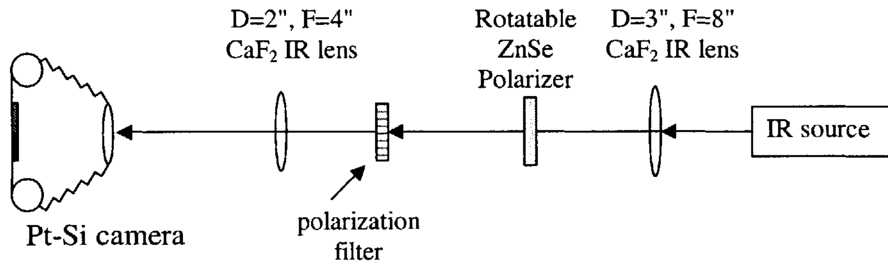

Figure 6-12: Optical set-up to characterize polarization filter samples

izer, only the polarization sub-filter whose orientation is parallel to this direction is transmissive. (Text lines in the images are parallel to the optical table plane.) When the relative orientation of the polarization filter to the optical table plane is 45°, light transmits only partially, while it is not transmitted with a 90° relative orientation. The current to the source, I, was fixed at 1.0Åduring the measurement. θ is the orientation angle of the ZnSe polarizer, measured clockwise seen from the camera with respect to the normal to the optical table. The diagram on the left displays the structure of the polarization sub-filters.

6.3 Multispectral and Polarization Filters in Mechanical Contact

6.3.1 Measured results

Figure 6-14 shows the FTIR measurement results of individual combinations of spectral waveband and polarization orientation, when a multispectral filter and a polarization filter sample are placed in mechanical contact. Columns correspond to different polarization orientations and rows represent measurements using different spectral sub-filters. λ_1, λ_2 and λ_3 denote a waveband of $3.0 - 4.0\mu$m, $3.5 - 4.5\mu$m and

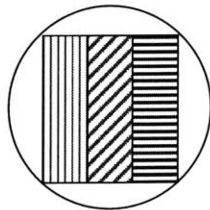

polarization sub-filter

$\theta=0^{\circ}$

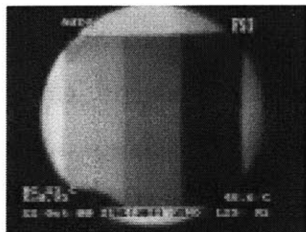

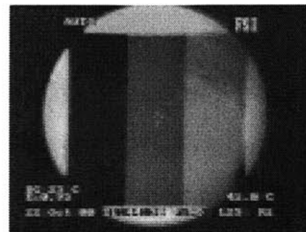

$\theta=90^{\circ}$

$\theta=45^{\circ}$

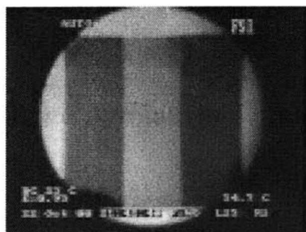

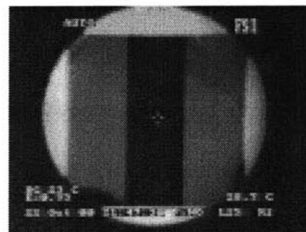

$\theta=135^{\circ}$

Figure 6-13: Transmission images of the polarization filter at different polarizer orientation

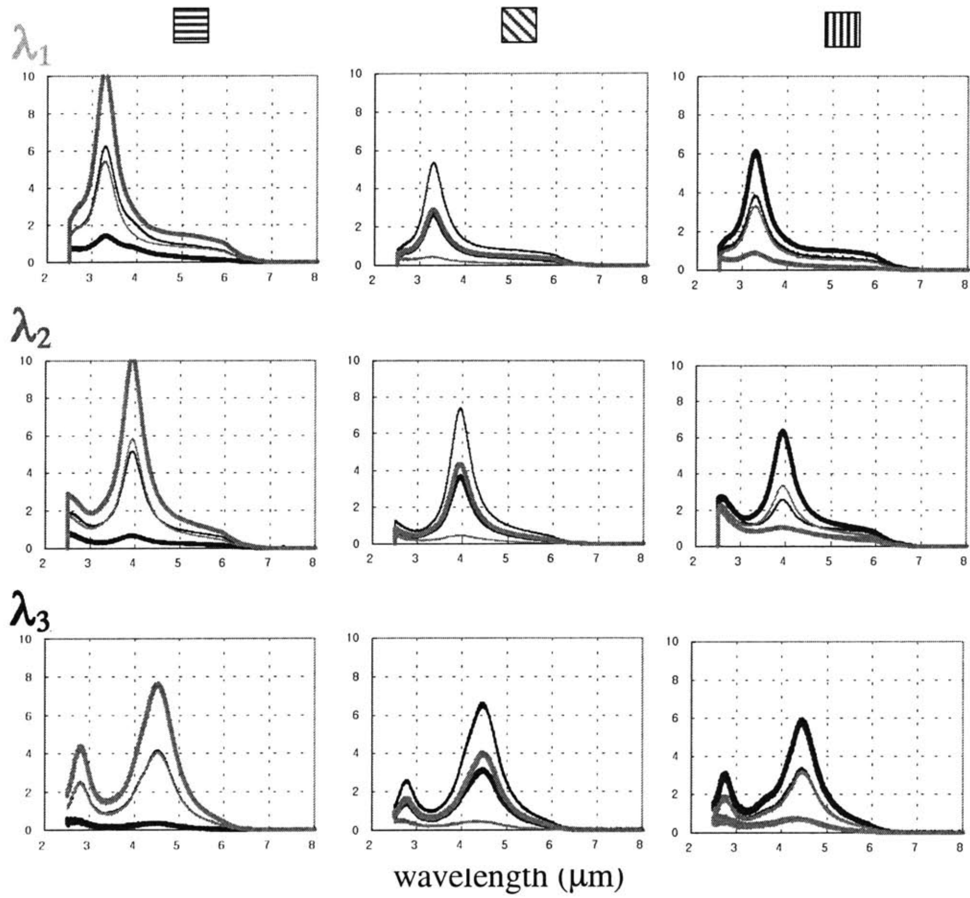

Figure 6-14: Measured results using FTIR for all combinations of multispectral pass-bands and polarization filter orientations

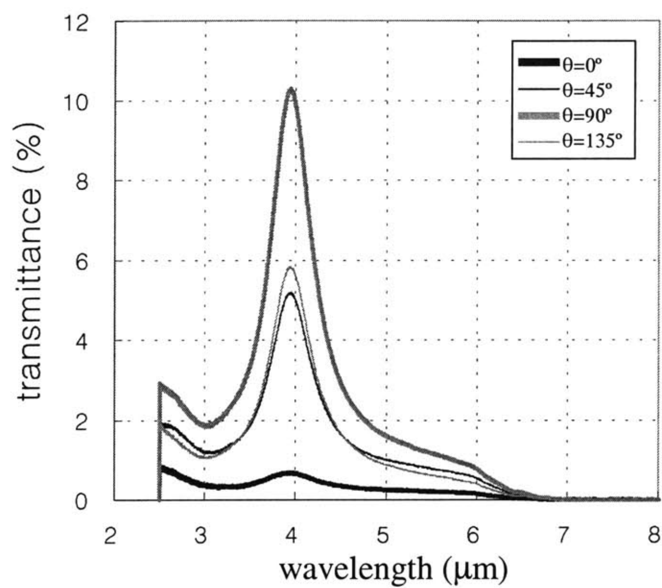

Figure 6-15: Intensity as a function of wavelength for the subpixel corresponding to horizontal polarization and $3.5 - 4.5\mu m$ waveband with source polarization angle θ

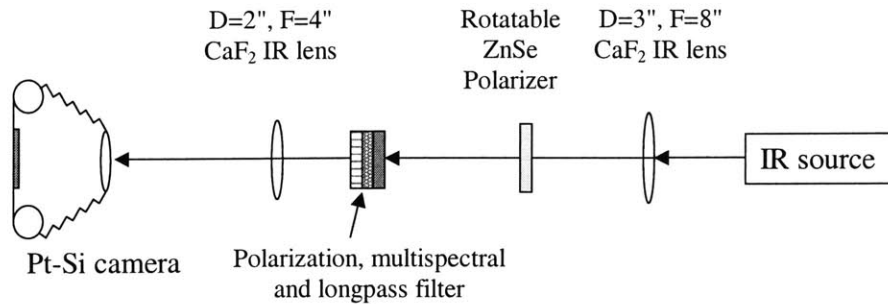

Figure 6-16: Optical set-up for multispectral polarization filter samples

$4.0 - 5.0\mu$m, respectively. An expanded transmittance characteristic for a sub-filter corresponding to the horizontal polarization and $3.5 - 4.5\mu$m waveband is shown in Figure 6-15. At the peak, the extinction ratio is 15.2, including the effect of the ZnSe polarizer. Since the extinction ratio due to the combined effect of the ZnSe polarizer and the FTIR system is 1.72 (from Figure 6-8), net extinction ratio of the sandwiched multispectral polarization sample is 8.84.

6.3.2 Characterization with the Pt-Si camera

Figure 6-16 is the top view of the optical set-up used to characterize multispectral and polarization filters in mechanical contact. The longpass filter, described in Section 6.1.2, was placed in mechanical contact with multispectral and polarization filters. The ZnSe polarizer was inserted and rotated to change the polarization state of the source.

Figure 6-17 shows the transmission images of the multispectral and polarization filters in mechanical contact, measured at different source temperatures. As expected, a checker-board pattern can be observed in the image. Each of the pixels corresponds to a set of spectral passband and polarization orientation $(\lambda_i, p_j)_{i,j=1,2,3}$, with i and j as a respective index.

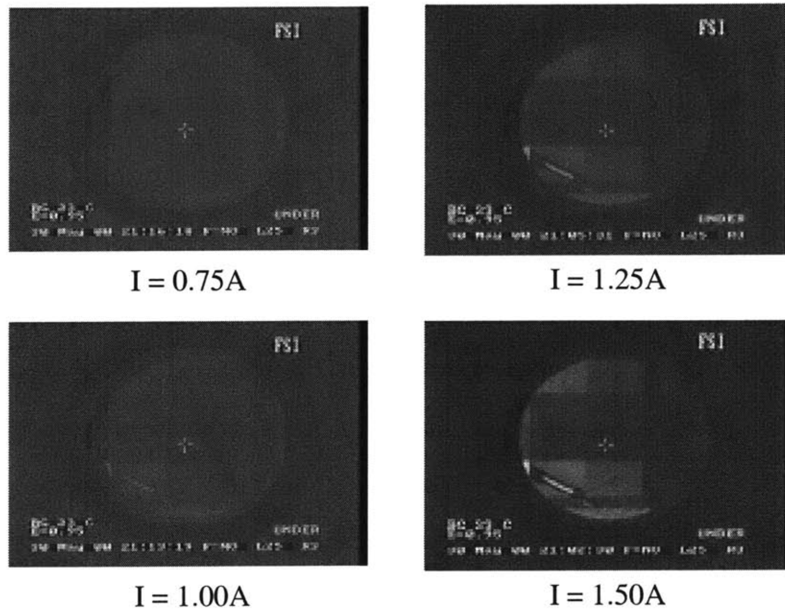

Figure 6-17: Transmission images of multispectral and polarization filters at different source temperatures

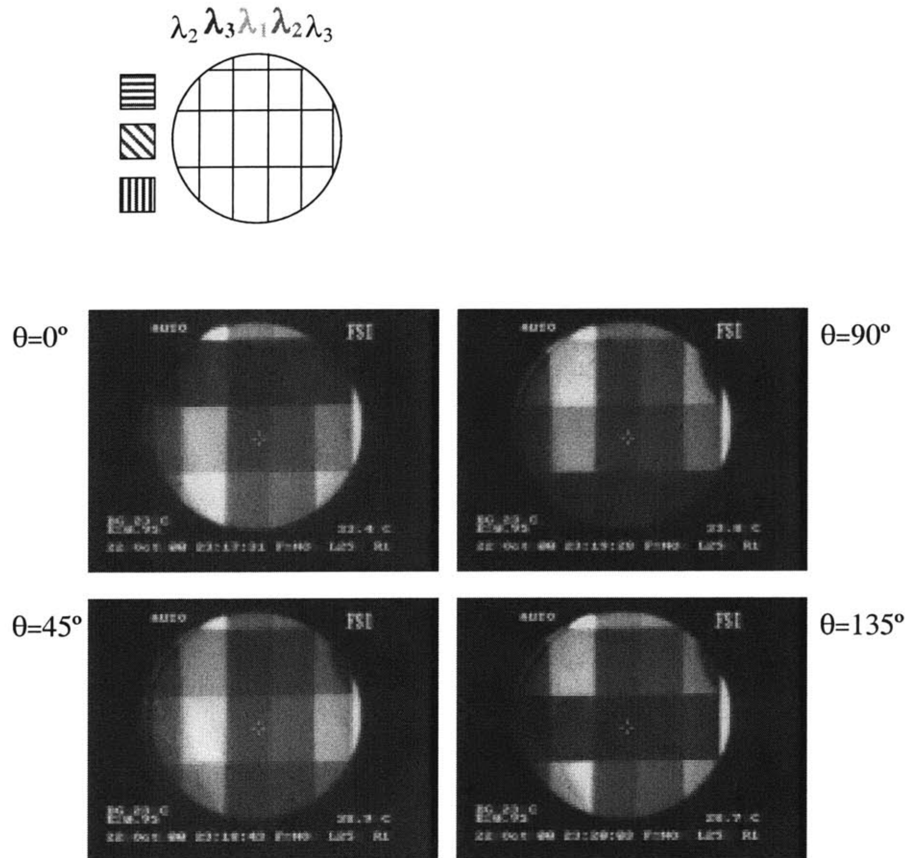

Figure 6-18: Transmission images of the multispectral and polarization filters in mechanical contact at different polarizer orientation

Figure 6-18, on the other hand, shows the transmission images at different orientation angles of the ZnSe polarizer. The current to the source, I, was fixed at 1.25A, 25% more than the one used to measure the polarization filter alone. This is because available power is reduced by mechanically contacting two filters. θ is the orientation angle of the ZnSe polarizer, measured anti-clockwise seen from the camera with respect to the normal to the optical table plane. The diagram on the left represents the structure of the multispectral and polarization sub-filters.

Chapter 7

Future Directions and Concluding Remarks

7.1 Future Direction

7.1.1 Flat Transmittance Characteristic of the Polarization Filter

The best approach to achieve both high and flat transmittance for the polarization filter is to use smaller pitch. In Figure 5-4, the simulated transmittance characteristics with 0.5μm pitch was compared with the results using 2.0μm pitch over Al/Nb/Ti (200Å/4500Å/500Å) gratings on a Si substrate.

If such a small pitch is not available, the transmittance characteristics of a wire-grid polarization filter may be flattened by combining metal gratings of different pitches in one unit period. Figure 7-1 shows two examples obtained from simulation, where one unit period of the grating contains 10 lines of 1.0μm pitch and 5 lines of 2.0μm pitch. It is clear from the figures that the transmittance characteristics can be made flat by introducing multiple pitches, the trade-off of which is reduced transmittance.

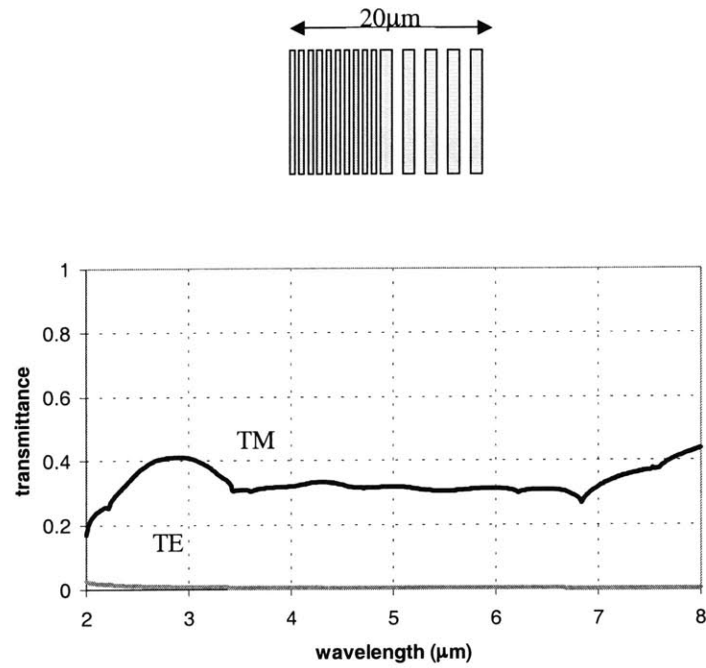

Figure 7-1: Transmittance of the metal wire-grid grating of multiple linewidths

7.1.2 Two Polarizers in Series

The performance of a polarizer can be improved by putting multiple polarizers in series[64]. The polarization contrast can be improved by integrating two wire-grid polarizers on the opposite sides of a substrate and putting it in mechanical contact with a multispectral filter. The alignment between polarizers will be a critical issue in this approach. Another disadvantage of this approach is that the loss of the system becomes more than double, compared to the system based on just one layer of polarizer.

7.1.3 Hyperspectral Filter Using Non-Uniformity

It was observed that the non-uniformity in the dry-etching process creates peak wavelength shifts in the response of the multispectral filter. This can be used to design a new kind of hyperspectral filter. The practicality of this scheme depends on the scale of the wavelength shift that it can produce and the wavelength resolution that the detector array should offer. The non-uniformity may be created by, for example, oblique deposition of multilayer films[65, 66], where bandpass filters of continuous spectrum can be obtained.

7.1.4 Integrated Multispectral Polarization Filter

Multispectral and polarization filters were initially to be integrated on a same side of a Si substrate. The contact between the optical mask and substrate for a polarization filter worsens when the polarization filter is fabricated on top of the multispectral interference filter. Besides, higher-order diffraction from the polarization filter causes multiple reflection inside the multispectral filter and makes an additional noise. On the other hand, deposition of multi-layer interference films on top of the polarization filter de-planarizes the multispectral filter and destroys its characteristics. In addition, building multispectral and polarization filters on a same side of a substrate is accompanied by a coupled effect of waveguide and grating. This is called guided-mode resonance effects and usually produces sharp variations in the intensity of the

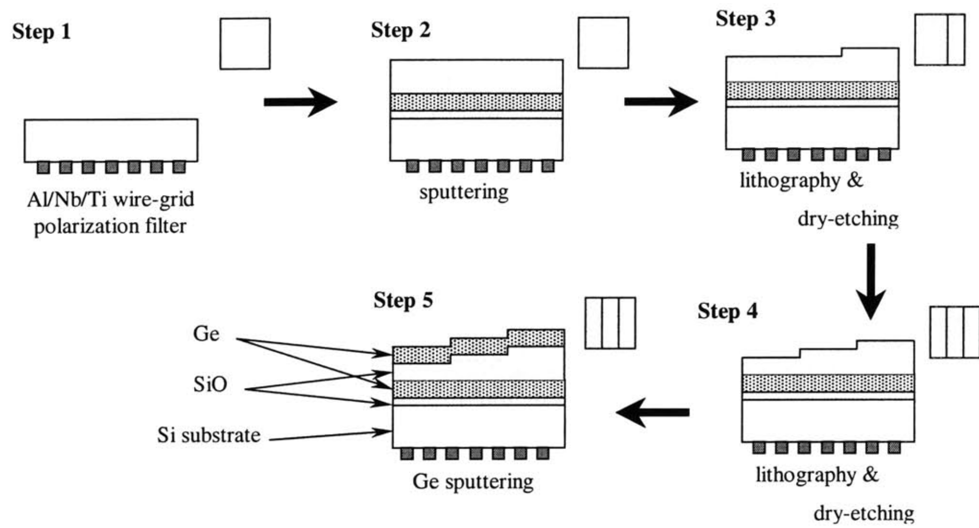

Figure 7-2: Processing flowchart for the triple-decker spectral polarizer plate on a common substrate

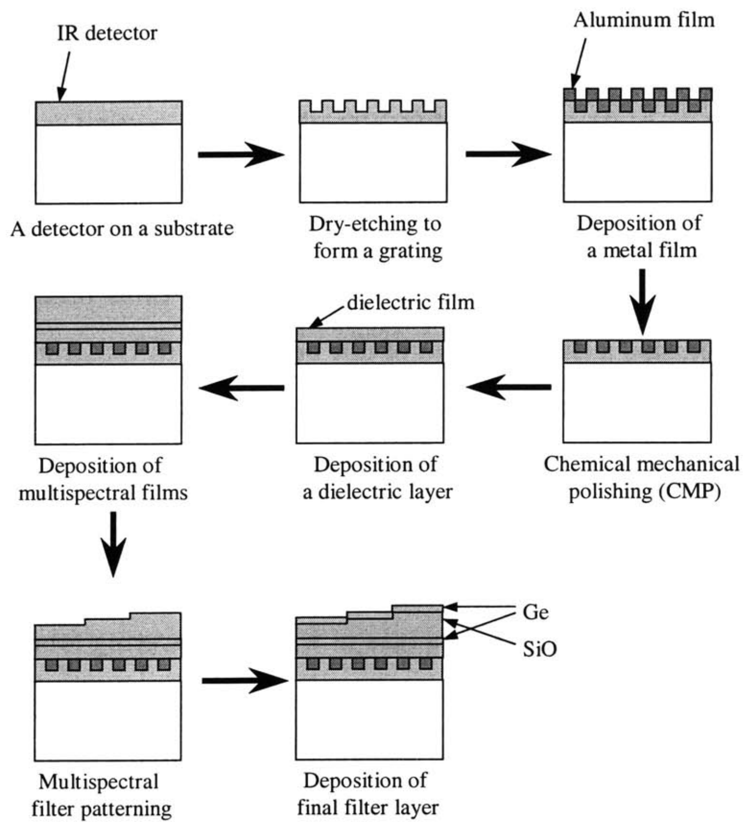

Figure 7-3: Processing flowchart to integrate the triple-decker spectral polarizer to a sensor on a single substrate

propagating waves[67, 68]. Therefore, instead of direct integration of multispectral and polarization filters on a same side, fabricating them on the opposite sides of a substrate may be more practical.

Figure 7-2 represents the processing flowchart for triple-decker design that implements the 4-layer multispectral filters on one side and the wire-grid polarization filter on the other side of the substrate. In Step 1, an Al/Nb/Ti wire-grid polarization filter can be fabricated on the backside of a double-side polished Si substrate. The polarization filter may have to be fabricated first, because this step requires a flat surface. In Step 2, three layers of SiO/Ge/SiO are deposited on the entire front side of the substrate. Steps 3 and 4 involve optical lithography, followed by selective dry-etching of the upper SiO layer to define the three multispectral sub-filters. In Step 5, the uppermost Ge layer is deposited on top of the three previous layers. This approach, however, has a disadvantage of not being able to integrate the filter plate to a detector on a common substrate.

To tackle this problem, a new approach may be taken as shown in Figure 7-3 conceptually. In this approach, a grating is first fabricated on top of a detector, which is followed by the deposition of polarization filter materials, such as aluminum or gold. The detector should be of a structure in which the grating fabrication does not degrade its performance. Chemical mechanical polishing (CMP) step then removes residual grating materials. Before multispectral films are deposited and patterned, a decoupling layer may be needed to minimize the crosstalk effects between multispectral and polarization filters. The thickness of this decoupling layer should be chosen such that this decoupling layer does not change the multispectral filter characteristic. Difficult this may be, it is interesting to note that adding an SiO layer to the bottom of the optimized 3-layer structure for sapphire substrates does not change the spectral characteristics. This means that such a layer could exist under certain conditions. At the same time, the decoupling layer should be thin, so that the light of higher-order diffraction does not pass into the neighboring pixels, in case that higher-order diffraction is present in the system because of a large pixel used in the wire-grid grating.

7.2 Concluding Remarks

In this thesis work, multispectral and polarization filters were designed and fabricated for the $3 - 5\mu m$ waveband. In this initial phase of a broader study, a discrete-component approach was taken first to establish the operational feasibility of the sensor concept based on spectral and polarimetric characteristics as discriminants in the $3 - 5\mu m$ waveband. A single-pixel prototype sensor was introduced. The characterization was performed using an FTIR spectrometer and a Pt-Si thermal imaging camera. The experimental results with the single-pixel device show excellent agreement with theoretical predictions. Currently, a 12×12 pixel array of multispectral filters and a corresponding array of polarization filters are being fabricated.

In the short term, the multispectral and polarization filters can be integrated on a common substrate and the pixel count can be increased up to an array of 64×64 and the spectral polarizer plate retrofitted to an off-the-shelf camera. The spectral polarizer plate can be mechanically contacted to detector array with the sensor cooled by Sterling engine of camera. It would also be possible to collaborate with a camera manufacturer on camera modification and packaging. This sensor can be calibrated and tested with a set of natural and artificial scenes and the data processing will be done off-chip in a personal computer.

In the long term, full integration of the spectral polarizer filter layer, detector array, VLSI pre-processor, with a Sterling engine into a single package should be attempted. This system should be characterized with natural and artificial scenes and sensor fusion algorithm implemented on data from the system to demonstrate contrast enhancement. This sensor system can be delivered for field-testing, e.g. tower, aircraft, and spacecraft data.

Appendix A

Program Code to Design a Multi-layer Interference Filter Based on Simulated Annealing

A.1 FilterOptimization.c - non-dispersive materials

```
#include <stdio.h>
#include <math.h>
#include <stdlib.h>
#include "../Vargle/vargle.h"
#include "../mylibrary/athena.h"
#include "../mylibrary/FilterOptimization.h"

double ErrorEvaluation(float a, float b, double *c, double d, double e, int f);

/* Revised on 6/13/00 */                                                    10

main(argc, argv)
        int argc;
        char **argv;
{
int i;

float WavelengthMin, WavelengthMax, WavelengthStep;
float RefractiveIndex1, RefractiveIndex2, RefractiveIndexS;
unsigned int NumLayers, LoopNumber;                                         20
float TargetThicknessMin, TargetThicknessMax, TargetSpectrumMin, \
```

```
        TargetSpectrumMax, CenterWavelength;
char *FileName1, *FileName2;
float WritingTolerance, Deviation;

PropagationMatrix PM, PM1, PM2, PMinit = { 1,0, 0,0, 0,0, 1,0 };
                                    /*      [0,0][0,1][1,0][1,1] */

double *FilmThickness, *FilmThicknessEstimate, *FilmThicknessCache;
double *RefractiveIndexLayer1, *RefractiveIndexLayer2, *Transmittance;
unsigned int NumTransmittance, Interface;
int TransmittanceCount;

        /* Layer 1 is the one that faces the air */

int LoopSimulatedAnnealing;
double Wavelength; /* in um */

double kT, StatisticMeasure, AnnealRate, AnnealConst, RandomNumber, dummy=0;
int NumberOfChange = 0;

double Error = 10000., MeasuredError;

FILE *fp_out1, *fp_out2;

VargInit();
VargErrorSetErrorFunq (VargErrorPrintAndExit);
VargReadFile(argv[1]);

WavelengthMin = VargAccessVfloat("WavelengthMin");
WavelengthMax = VargAccessVfloat("WavelengthMax");
NumTransmittance = VargAccessVint("NumTransmittance");
RefractiveIndex1 = VargAccessVfloat("RefractiveIndex1");
RefractiveIndex2 = VargAccessVfloat("RefractiveIndex2");
RefractiveIndexS = VargAccessVfloat("RefractiveIndexS");
NumLayers = VargAccessVint("NumLayers");
TargetThicknessMin = VargAccessVfloat("TargetThicknessMin");
TargetThicknessMax = VargAccessVfloat("TargetThicknessMax");
TargetSpectrumMin = VargAccessVfloat("TargetSpectrumMin");
TargetSpectrumMax = VargAccessVfloat("TargetSpectrumMax");
CenterWavelength = VargAccessVfloat("CenterWavelength");
AnnealRate = VargAccessVfloat("AnnealRate");
AnnealConst = VargAccessVfloat("AnnealConst");
FileName1 = VargAccessVstring("FileName1");
FileName2 = VargAccessVstring("FileName2");
LoopNumber = VargAccessVint("LoopNumber");
WritingTolerance = VargAccessVfloat("WritingTolerance");
Deviation = VargAccessVfloat("Deviation");

FilmThickness = (double *)malloc((NumLayers+1) * sizeof(double));
FilmThicknessEstimate = (double *)malloc(NumLayers * sizeof(double));
FilmThicknessCache = (double *)malloc(NumLayers * sizeof(double));

RefractiveIndexLayer1 = (double *)malloc((NumLayers+1) * sizeof(double));
RefractiveIndexLayer2 = (double *)malloc((NumLayers+1) * sizeof(double));
```

```
WavelengthStep = (WavelengthMax−WavelengthMin)/(double)NumTransmittance;
printf("\nSampling Number in the Spectrum:%d\n\n",(int)NumTransmittance);

Transmittance = (double *)malloc(NumTransmittance * sizeof(double));                    80

fp_out1 = fopen(FileName1,"w");
fclose(fp_out1);

FilmThicknessEstimate[0] = 0.;

/**********************************************************/
/*        .........    . beginning the loop .         ............ */
/**********************************************************/
                                                                                         90
for(Interface=0;Interface<=NumLayers;Interface++) {

        if (Interface==0){
                RefractiveIndexLayer1[Interface] = 1.0;
                RefractiveIndexLayer2[Interface] = RefractiveIndex1;
                /* Initialize refractive indices */

                if (!NumLayers)         /* Just in case */
                        RefractiveIndexLayer2[Interface] = RefractiveIndexS;
        } else if (Interface==NumLayers && !ISEVEN(NumLayers)){                          100
                RefractiveIndexLayer1[Interface] = RefractiveIndex1;
                RefractiveIndexLayer2[Interface] = RefractiveIndexS;
        } else if (Interface==NumLayers && ISEVEN(NumLayers)){
                RefractiveIndexLayer1[Interface] = RefractiveIndex2;
                RefractiveIndexLayer2[Interface] = RefractiveIndexS;
        }  else{
                if (!ISEVEN(Interface)){
                        RefractiveIndexLayer1[Interface] = RefractiveIndex1;
                        RefractiveIndexLayer2[Interface] = RefractiveIndex2;
                } else {                                                                 110
                        RefractiveIndexLayer1[Interface] = RefractiveIndex2;
                        RefractiveIndexLayer2[Interface] = RefractiveIndex1;
                }
        }
        if (Interface){
                FilmThicknessEstimate[Interface−1] = 0;
        }

for(LoopSimulatedAnnealing=0;LoopSimulatedAnnealing<LoopNumber;\
                                LoopSimulatedAnnealing++) {                              120
        RandomArray(FilmThickness,NumLayers+1,\
                (TargetThicknessMax−TargetThicknessMin),0,FilmThicknessEstimate);
        FilmThickness[0] = 0; /* .. forces it to be zero .. */

        for(TransmittanceCount=0,Wavelength=WavelengthMin; \
                        TransmittanceCount<NumTransmittance;TransmittanceCount++) {
                Wavelength += WavelengthStep;
                PM1 = PMinit;
```

```
		for(Interface=0;Interface<=NumLayers;Interface++) {                          130
			/* Assumes no absorption by 0,0 */
			PM2 = PropMatrixMul(PMinit,Wavelength, \
				RefractiveIndexLayer1[Interface], \
				RefractiveIndexLayer2[Interface],0, \
				0,FilmThickness[Interface],Interface);
			PM1 = ComplexMatrixMul(PM1,PM2);
		} /* for - Interface */
		Transmittance[TransmittanceCount] = \
			1-ComplexNorm2(PM1.at[1][0])/ComplexNorm2(PM1.at[0][0]);
	} /* for - Wavelength */                                                             140
	MeasuredError = WavelengthStep * ErrorEvaluation(TargetSpectrumMin, \
				TargetSpectrumMax,Transmittance,WavelengthMin, \
				WavelengthStep,NumTransmittance);

	kT = AnnealRate / (NumberOfChange*AnnealConst + 1);
	StatisticMeasure = exp(-MeasuredError/kT);
	RandomArray(&RandomNumber,1,1,0,&dummy);
	if (Error > MeasuredError || StatisticMeasure > RandomNumber){
		fprintf(stderr,"Loop:%7d\t\tError:%f\r",LoopSimulatedAnnealing,Error);
		if ( fabs(Error-MeasuredError) > WritingTolerance ){                         150
			fp_out1 = fopen(FileName1,"a");
			fprintf(fp_out1,"Error:%f\t",MeasuredError);
			for(Interface=0;Interface<NumLayers;Interface++){
				FilmThicknessCache[Interface] = FilmThickness[Interface+1];
				fprintf(fp_out1,"%f   ",FilmThicknessCache[Interface]);
			}
			fprintf(fp_out1,"\n");
			fclose(fp_out1);
		}
		fp_out2 = fopen(FileName2,"w");                                              160
		for(i=0;i<TransmittanceCount;i++)
			fprintf(fp_out2,"%f\t%f\n", \
				WavelengthMin+WavelengthStep*i,Transmittance[i]);
		fclose(fp_out2);

		Error = MeasuredError;
		NumberOfChange++; /* Assign New Values */
	} /* else start anew */
} /* for - Simulated annealing */
printf("\n\n");                                                                          170

free(FilmThickness); free(FilmThicknessCache);
free(Transmittance); free(RefractiveIndexLayer1);
free(RefractiveIndexLayer2);
} /* end of main */

double ErrorEvaluation(float TargetMin, float TargetMax, double *Transmittance, \
		double WavelengthMin, double WavelengthStep, int NumTransmittance)
{
	double x, y;                                                                     180
	double c1 = (TargetMax+TargetMin)/2, c2 = (TargetMax-TargetMin)/2;

	int i;
```

```
        for(i=0,x=0;i<NumTransmittance;i++){
                y = WavelengthMin + (double)i*WavelengthStep;
                if (y>TargetMin && y<TargetMax)
                        /* x += SQ(SINC((y-c1)/c2)-Transmittance[i]); */
                                /* using sinc measure instead of square */
                        x += SQ(1-Transmittance[i]);                                    190
                else
                        x += SQ(Transmittance[i]);
        } /* end of for */

        return(sqrt(x));
} /* end of ErrorEvaluation */
```

A.2 FilterOptimization.c - dispersive materials

```
#include <stdio.h>
#include <math.h>
#include <stdlib.h>
#include <strings.h>
#include <ctype.h>
#include "../Vargle/vargle.h"
#include "../mylibrary/athena.h"
#include "../mylibrary/FilterOptimization.h"
#include "dataD.h"
                                                                                        10
double ErrorEvaluation(float a, float b, double *c, double d, double e, int f);
double GetIndex(double WavelengthInLoop, int Material);
double GetAbsorption(double WavelengthInLoop, int Material);

main()
{
int i, j, Letter, LineIndex;
int Material1, Material2, MaterialS;

float WavelengthMin, WavelengthMax, TargetMin, TargetMax, CenterWavelength;            20
float RefractiveIndexA, RefractiveIndex1, RefractiveIndex2, RefractiveIndexS;
float Material1Factor, Material2Factor, Material1AbsorptionFactor, \
        Material2AbsorptionFactor, Criterion;
unsigned int NumBaseLayers, NumAddLayers;
char *Material1Str, *Material2Str, *MaterialSStr;
char *OptFileName, *TransFileName;

PropagationMatrix PM, PM1, PM2, PMinit = { 1,0, 0,0, 0,0, 1,0 };
                                        /*      [0,0][0,1][1,0][1,1] */
                                                                                        30
double Wavelength, WavelengthStep;
double n1, n2, ns, k1, k2, ks;
double *FilmThickness, TotalThickness;
double *RefractiveIndexLayer1, *RefractiveIndexLayer2, *AbsorptionCoeffLayer1, \
        *AbsorptionCoeffLayer2;
```

```
unsigned int NumTransmittance, NumLayers, Interface, Reset;
double *Transmittance;
int TransmittanceCount;
char ThicknessFactorString[256], EachLine[512], LayerThickness[16], \
        UnfoldedStructure[2048] = "";                                    40
double ThicknessFactor, MeasuredError;

FILE *fp_out, *fp_in;

/***********************************************/

VargInit();
VargErrorSetErrorFunq (VargErrorPrintAndExit);
VargReadFile("./SeeD.arg");
                                                                         50
WavelengthMin = VargAccessVfloat("WavelengthMin");
WavelengthMax = VargAccessVfloat("WavelengthMax");
TargetMin = VargAccessVfloat("TargetMin");
TargetMax = VargAccessVfloat("TargetMax");
CenterWavelength = VargAccessVfloat("CenterWavelength");
NumTransmittance = VargAccessVint("NumTransmittance");
Criterion = VargAccessVfloat("Criterion");
NumLayers = VargAccessVint("NumLayers");
Material1Str = VargAccessVstring("Material1Str");
Material2Str = VargAccessVstring("Material2Str");                       60
MaterialSStr = VargAccessVstring("MaterialSStr");
Material1Factor = VargAccessVfloat("Material1Factor");
Material2Factor = VargAccessVfloat("Material2Factor");
Material1AbsorptionFactor = VargAccessVfloat("Material1AbsorptionFactor");
Material2AbsorptionFactor = VargAccessVfloat("Material2AbsorptionFactor");
OptFileName = VargAccessVstring("OptFileName");
TransFileName = VargAccessVstring("TransFileName");
Reset = VargAccessVint("Reset");

/***********************************************/                        70

WavelengthStep = (WavelengthMax-WavelengthMin)/(double)NumTransmittance;

printf("\n\nSampling Number in the Spectrum:%d\n",(int)NumTransmittance);

Transmittance = (double *)malloc(NumTransmittance * sizeof(double));

/***********************************************/

FilmThickness = (double *)malloc((NumLayers+1) * sizeof(double));        80

RefractiveIndexLayer1 = (double *)malloc((NumLayers+1) * sizeof(double));
RefractiveIndexLayer2 = (double *)malloc((NumLayers+1) * sizeof(double));
AbsorptionCoeffLayer1 = (double *)malloc((NumLayers+1) * sizeof(double));
AbsorptionCoeffLayer2 = (double *)malloc((NumLayers+1) * sizeof(double));

FilmThickness[0] = 0.;          /* .. the 1st layer faces air.. */

Material1 = GetMaterial(Material1Str);
```

```
Material2 = GetMaterial(Material2Str);                                          90
MaterialS = GetMaterial(MaterialSStr);

/***********************************************/
/***********************************************/

fp_in = fopen(OptFileName,"r");
for(LineIndex=0;fgets(EachLine,512,fp_in);LineIndex++){

        printf("\nStructure analysis given the thicknesses corresponding all layers \
                \nSet NumLayers = NumBaseLayers & NumAddLayers = 0\n\n");       100

        Letter=0;
        if (isalpha(EachLine[0]))        /* For .out file */
        for(;isalnum(EachLine[Letter]) || EachLine[Letter]=='.' || EachLine[Letter]==':'; \
                        Letter++);

        for(;!(isdigit(EachLine[Letter])||EachLine[Letter]=='.'); \
                        Letter++); /* remove spaces */
        for(Interface=0;Interface<NumLayers;Interface++){
                for(j=0;(isdigit(EachLine[Letter])||EachLine[Letter]=='.');Letter++,j++)  110
                        LayerThickness[j] = EachLine[Letter];

                for(;!(isdigit(EachLine[Letter])||EachLine[Letter]=='.');Letter++)
                        strcat(LayerThickness,"\0");
                FilmThickness[Interface+1] = atof(LayerThickness);
                strcpy(LayerThickness,"");
                printf("\t%d:%f(um)\n ",Interface+1,FilmThickness[Interface+1]);
        } printf("\n");

        for(TransmittanceCount=0,Wavelength=WavelengthMin; \                    120
                TransmittanceCount<NumTransmittance;TransmittanceCount++, \
                Wavelength+=WavelengthStep) {
                n1 = GetIndex(Wavelength,Material1);
                n2 = GetIndex(Wavelength,Material2);
                ns = GetIndex(Wavelength,MaterialS);

                k1 = GetAbsorption(Wavelength,Material1)*Reset;
                k2 = GetAbsorption(Wavelength,Material2)*Reset;
                ks = GetAbsorption(Wavelength,MaterialS)*Reset;
                                                                                130
                RefractiveIndexLayer1[0] = 1.0;
                RefractiveIndexLayer2[NumLayers] = ns;
                AbsorptionCoeffLayer1[0] = 0.0;
                AbsorptionCoeffLayer2[NumLayers] = ks; /* redundant */
                for(Interface=0;Interface<=NumLayers;Interface++){
                        if (Interface==0){
                                RefractiveIndexLayer1[Interface] = 1.0;
                                RefractiveIndexLayer2[Interface] = n1*Material1Factor;
                                AbsorptionCoeffLayer1[Interface] = 0.0;
                                AbsorptionCoeffLayer2[Interface] = k1*Material1AbsorptionFactor; 140
                                /* Initialize refractive indices, Material1 faces air */
                                if (!NumLayers){        /* Just in case */
                                        RefractiveIndexLayer2[Interface] = ns;
```

```
                        AbsorptionCoeffLayer2[Interface] = ks;
                    }
                } else if (Interface==NumLayers && !ISEVEN(NumLayers)){
                    RefractiveIndexLayer1[Interface] = n1*Material1Factor;
                    RefractiveIndexLayer2[Interface] = ns;
                    AbsorptionCoeffLayer1[Interface] = k1*Material1AbsorptionFactor;
                    AbsorptionCoeffLayer2[Interface] = ks;                          150
                } else if (Interface==NumLayers && ISEVEN(NumLayers)){
                    RefractiveIndexLayer1[Interface] = n2*Material2Factor;
                    RefractiveIndexLayer2[Interface] = ns;
                    AbsorptionCoeffLayer1[Interface] = k2*Material2AbsorptionFactor;
                    AbsorptionCoeffLayer2[Interface] = ks;
                } else {
                    if (!ISEVEN(Interface)){
                        RefractiveIndexLayer1[Interface] = n1*Material1Factor;
                        RefractiveIndexLayer2[Interface] = n2*Material2Factor;
                        AbsorptionCoeffLayer1[Interface] = \                        160
                            k1*Material1AbsorptionFactor;
                        AbsorptionCoeffLayer2[Interface] = \
                            k2*Material2AbsorptionFactor;
                    } else {
                        RefractiveIndexLayer1[Interface] = n2*Material2Factor;
                        RefractiveIndexLayer2[Interface] = n1*Material1Factor;
                        AbsorptionCoeffLayer1[Interface] = \
                            k2*Material2AbsorptionFactor;
                        AbsorptionCoeffLayer2[Interface] = \
                            k1*Material1AbsorptionFactor;                           170
                    }
                }
            }

/****************************************************************************/
/* ................................ calculation ................................ */
/****************************************************************************/

            PM1 = PMinit;
                                                                                    180
            for(Interface=0;Interface<=NumLayers;Interface++) {
                PM2 = PropMatrixMul(PM1,Wavelength,RefractiveIndexLayer1[Interface], \
                    RefractiveIndexLayer2[Interface], AbsorptionCoeffLayer1[Interface], \
                    AbsorptionCoeffLayer2[Interface], FilmThickness[Interface],Interface);
                PM1 = ComplexMatrixAsgn(PM2);
            }       /* Interface loop */

            Transmittance[TransmittanceCount] = \
                1 - ComplexNorm2(PM1.at[1][0])/ComplexNorm2(PM1.at[0][0]);
            if (Wavelength>8 && Wavelength<12){                                     190
                printf("Wavelength:%f,Transmittance:%f\n",Wavelength,\
                    Transmittance[TransmittanceCount]); getchar();
            }

/******************************************************************************/

        }       /* wavelength loop */
```

```
        printf("\n\nTotal Thickness of the Film:%2.3f (um)",TotalThickness);
        MeasuredError = ErrorEvaluation(TargetMin,TargetMax,Transmittance,WavelengthMin, \
                                        WavelengthStep,NumTransmittance);                 200
        printf("\n\nMeasured Error:%3.3f",MeasuredError);
        fp_out = fopen(TransFileName,"w");
        for(i=0;i<NumTransmittance;i++)
                fprintf(fp_out,"%f\t%f\n",WavelengthMin+i*WavelengthStep,Transmittance[i]);
        fclose(fp_out);
}       /* LineIndex loop */
fclose(fp_in);

free(FilmThickness); free(Transmittance);
free(RefractiveIndexLayer1); free(RefractiveIndexLayer2);                                  210
} /* end of main */

double GetIndex(double WavelengthInLoop, int Material)
{
        int i, n1, n2;
        double l1, l2, n;

        for(i=0;WavelengthInLoop >= RI[Material][i].wavelength;i++);
                n1 = i-1; l1 = RI[Material][n1].wavelength;
                n2 = I; l2 = RI[Material][n2].wavelength;                                  220

        if (l2 != l1)
                n = fabs(((WavelengthInLoop-l1)*RI[Material][n2].index + \
                        (l2-WavelengthInLoop)*RI[Material][n1].index)/(l2-l1));
        else
                n = RI[Material][n2].index;

        return(n);
}
                                                                                           230
double GetAbsorption(double WavelengthInLoop, int Material)
{
        int i, k1, k2;
        double difference, min, l1=0, l2=100, k;

        for(i=0;WavelengthInLoop >= AC[Material][i].wavelength;i++);
                k1 = i-1; l1 = AC[Material][k1].wavelength;
                k2 = i; l2 = AC[Material][k2].wavelength;
                if (l2 != l1)
                        k = ((WavelengthInLoop-l1)*AC[Material][k2].index +      \         240
                                (l2-WavelengthInLoop)*AC[Material][k1].index)/(l2-l1);
                else
                        k = AC[Material][k2].index;

        return(k);
}
```

A.3 MyMath.c

```
PropagationMatrix ComplexMatrixAsgn(PropagationMatrix a)
{
        PropagationMatrix x;

        x.at[0][0] = a.at[0][0]; x.at[0][1] = a.at[0][1];
        x.at[1][0] = a.at[1][0]; x.at[1][1] = a.at[1][1];
        return(x);
}

PropagationMatrix ComplexMatrixMul(PropagationMatrix a, PropagationMatrix b)        10
{
        PropagationMatrix c;

        c.at[0][0] = ComplexAdd(ComplexMul(a.at[0][0],b.at[0][0]),\
                                ComplexMul(a.at[0][1],b.at[1][0]));
        c.at[0][1] = ComplexAdd(ComplexMul(a.at[0][0],b.at[0][1]),\
                                ComplexMul(a.at[0][1],b.at[1][1]));
        c.at[1][0] = ComplexAdd(ComplexMul(a.at[1][0],b.at[0][0]),\
                                ComplexMul(a.at[1][1],b.at[1][0]));
        c.at[1][1] = ComplexAdd(ComplexMul(a.at[1][0],b.at[0][1]),\                  20
                                ComplexMul(a.at[1][1],b.at[1][1]));

        return(c);
}

PropagationMatrix PropMatrixMul(PropagationMatrix Matrix1stLayer, double wavelength, \
        double n1, double n2, double k1, double k2, double thickness, int layer)
{
        double delta, absorption, Coeff_reflection, Coeff_transmission;
        PropagationMatrix Matrix2ndLayer, MatrixBothLayers;                           30

        delta = (2*PI/wavelength)*n1*thickness;
        absorption = (2*PI/wavelength)*k1*thickness;
        if (!layer){
                delta = 0;      /* ..the first layer, facing air.. */
                absorption = 0;
        }

        Coeff_reflection = (n1-n2)/(n1+n2);
        Coeff_transmission = 2*n1/(n1+n2);                                            40

        Matrix2ndLayer.at[0][0] = \
                EXPJ(delta,1/Coeff_transmission*exp(-absorption));
        Matrix2ndLayer.at[0][1] = \
                EXPJ(delta,Coeff_reflection/Coeff_transmission*exp(-absorption));
        Matrix2ndLayer.at[1][0] = \
                EXPJ(-delta,Coeff_reflection/Coeff_transmission*exp(absorption));
        Matrix2ndLayer.at[1][1] = \
                EXPJ(-delta,1/Coeff_transmission*exp(absorption));
                                                                                      50
        MatrixBothLayers = ComplexMatrixMul(Matrix1stLayer,Matrix2ndLayer);
```

```
        /* MatrixBothLayers = Matrix1stLayer * Matrix2ndLayer */

    return(MatrixBothLayers);
}
```

A.4 FilterOptimization.h

```
typedef struct {
        double re; double im;
        }       zomplex;

typedef struct {
        zomplex at[2][2];
        }       PropagationMatrix;

#define MAX(x,y)    ((x>y)?(x):(y))
#define MIN(x,y)    ((x<y)?(x):(y))                                         10

/* Functions in the myran.c */
double ran1(long *idum);
double gasdev(long *idum, double deviation);
void RandomArray(double *randomarray, unsigned long nn, double amp, double off, double *avg);
void GasdevRandomArray(double *randomarray, unsigned long nn, double amp, double *avg, \
        double dev, double rangemin, double rangemax);
        /* ..assigns nn random numbers into the randomarray.. */

/* Functions in the mymath.c */                                             20
double SINC(double x);
double SQ(double x);
int MOD(int x, int y);
int ISEVEN(int x);
double ComplexNorm2(zomplex a);
zomplex EXPJ(double phase, double a);
zomplex ComplexAdd(zomplex a, zomplex b);
zomplex ComplexMul(zomplex a, zomplex b);
zomplex ComplexAsgn(zomplex a);
PropagationMatrix ComplexMatrixAsgn(PropagationMatrix a);                   30
PropagationMatrix ComplexMatrixMul(PropagationMatrix a, PropagationMatrix b);
        /* ..makes c equal to a*b */
PropagationMatrix PropMatrixMul(PropagationMatrix MatrixArray, double wavelength, \
        double n1, double n2, double k1, double k2, double thickness,int layer);
        /* Functions in the mystdio.c */
void printfM(char *a, PropagationMatrix b);
char *char2string(char a);
char *ParenthesisCall(int *Index, char *Structure);
int CountNumLayersInParenthesis(int *Index, char *Structure);
```

Appendix B

Material Data in Gsolver.ini

[Herzberger]

Sapphire: 0.5, 0, 0, 7.197, 0, 0.3322, 0, 0, 0, 0, 0.0843, 0, 0, 0, 0, 0

SiO(glass): 0.5, 0, 0, 3.00159, 0, 0.00325747, 0.00551215, 87.8937, 0, 0, 0.00467915, 0.0135121, 97.934, 0, 0, 0

Si: 1, -2.09e-005, 1.48e-007, 3.41696, 0, 0.138497, 0, 0, 0, 0, 0.028, 0, 0, 0, 0, 0.013924

Ge: 1, -6e-006, 5.3e-008, 3.99931, 0, 0.391707, 0, 0, 0, 0, 0.028, 0, 0, 0, 0, 0.163492

[Schott]

GaAsi: 10.9619, -0.00193929, -1.95263, 25.7853, -59.427, 27.0774

[Polynomial]

Cr: 1, 8.53411, -3.88007, -5.44815, 7.07702, -3.52238, 0.927452, -0.135284, 0.0102981, -0.000318461, 0, 32.3758, -73.18, 77.0718, -44.2716, 15.0905, -3.122, 0.383636, -0.0256806, 0.000719156

Nb: 1, 8.78394, -19.2199, 17.5196, -8.52405, 2.45611, -0.43114, 0.0451896, -0.00259315, 6.24972e-005, 0, 1.61626, 4.07416, -0.473913, -0.986596, 0.569919, -0.141852, 0.0185436, -0.00124056, 3.34319e-005

Ti-poly: 1, 6.50257, -9.10662, 7.81664, -3.86477, 1.1151, -0.191273, 0.0192206, -0.00104436, 2.36779e-005, 0, 77.7837, -120.62, 82.177, -31.1866, 7.18791, -1.02918, 0.0894348, -0.0043178, 8.88127e-005 Ti-electro: 1, 6.50257, -9.10662, 7.81664, -3.86477, 1.1151, -0.191273, 0.0192206, -0.00104436, 2.36779e-05, 0, 5.93504, -2.54822, -0.230844, 0.514401, -0.147589, 0.0169044, -0.000527311, -4.07426e-005, 2.50277e-006

Appendix C

Vendor Information

Virginia Semiconductors - Si wafers

http://www.virginiasemi.com/
1501 Powhatan Street
Fredericksburg, VA 22401-4647
Phone: (540) 373-2900
Fax: (540) 371-0371

Crystal Systems Inc. - Sapphire

http://www.crystalsystems.com/
27 Congress St., Salem, MA 01970
Tel: 508-745-0088; fax: 508-744-5049

Kurt J. Lesker Inc. - SiO and Ge sputtering Targets

http://www.lesker.com/
1515 Worthington Avenue
Clairton, PA 15025
TEL 412/233-4200, 800/245-1656
FAX 412/233-4275

Corion Inc. - Longpass Optical Filter

http://www.corion.com/
8 East Forge Parkway
Franklin, MA 02038-3148
Telephone: (508) 528-4411/(800) 598-6783
Fax: (508) 520-7583

Advanced Reproduction Inc. - Optical Mask for Multispectral Filter

http://www.advancerepro.com/
100 Flagship Drive

North Andover, MA 01845
Phone: (978) 685-2911
Fax: (978) 685-1771

Photronics Inc. - E-beam Mask for Polarization Filter
http://www.photronics.com/
15 Secor Road
Brookfield, CT 06804

Oriel Instruments Inc. - Optical Components for Characterization (broadband IR source, power supply etc.)
http://www.oriel.com/
150 Long Beach Blvd.
Stratford, CT 06615 USA
Tel (203) 377-8282
Fax (203) 378-2457

Spectra Tech Inc. - ZnSe wire-grid polarizer
http://www.spectra-tech.com
2 Research Drive
Shelton, CT 06484-0869
Tel 1-800-843-3847

Bibliography

[1] R. D. Tooley. Man-made target detection using infrared polarization. *Proc. of SPIE, vol. 1166 Polarization Considerations for Optical Systems II*, page 33, 1989.

[2] T. J. Rogne, F. G. Smith, and J. E. Rice. Passive target detection using polarized components of infrared signature. *Proc. of SPIE, vol. 1317 Polarimetry: Radar, Infrared, Visible, Ultraviolet, and X-Ray*, page 242, 1990.

[3] T. J Rogne, R. Maxwell, J. Nicoll, and R. Legault. Ir polarization for target cuing. *Proc. IRIS, Passive Sensors*, 1:323, 1997.

[4] M. J. Duggin, W. G. Egan, and J. Gregory. Measurements of polarization of targets of differing albedo and shadow depth. *Proc. of SPIE, vol. 3699 Targets and Backgrounds: Characterization and Representation V*, page 27, 1999.

[5] W. G. Egan. Enhancement of optical detectability with polarization. *Proc. of SPIE, vol. 3699 Targets and Backgrounds: Characterization and Representation V*, page 38, 1999.

[6] G. P. Können. *Polarized Light in Nature.* Cambridge University Press, 1985.

[7] N. Berova, K. Nakanishi, and R. Woody. *Circular Dichroism : Principles and Applications.* Wiley, 2nd edition, 2000.

[8] G. U. Spohr. *Messung der Polarisation von Streulicht über Wasserflachen, Ph.D. Thesis.* 1978.

[9] O. Sandus. A review of emission polarization. *Appl. Opt.*, 4:1634, 1965.

[10] D. Clarke and J. F. Grainger. *Polarized Light and Optical Measurement.* Pergamon Press, 1971.

[11] W. G. Egan. Proposed design of an imaging spectropolarimeter/photopolarimeter for remote sensing of earth resources. *Opt. Eng.*, 25(10):1155, 1986.

[12] W. G. Egan. Polarization in remote sensing ii. *Proc. of SPIE, vol. 1166 Polarization Considerations for Optical Systems II*, page 23, 1989.

[13] W. G. Egan. Polarization in remote sensing. *Proc. of SPIE, vol. 1747 Polarization and Remote Sensing*, page 2, 1992.

[14] L. D. Travis. Remote sensing of aerosols with the earth observing scanning polarimeter. *Proc. of SPIE, vol. 1747 Polarization and Remote Sensing*, page 154, 1992.

[15] P. Y. Deschamps, M. Herman, A. Podaire, and A. Ratier. The polder instrument: Mission objectives. *Proc. of SPIE, vol. 1747 Polarization and Remote Sensing*, page 72, 1992.

[16] D. A. Glenar, J. J. Hillman, B. Saif, and J. Bergstrahl. Polaris ii: an acousto-optic imaging spectropolarimeter for ground-based astronomy. *Proc. of SPIE, vol. 1747 Polarization and Remote Sensing*, page 92, 1992.

[17] D. H. Goldstein and R. A. Chipman. Infrared spectropolarimeter. *U.S. Patent*, #5,045,701, 1991.

[18] D. B. Chenault and R. A. Chipman. Infrared spectropolarimetry. *Proc. of SPIE, vol. 1166 Polarization Considerations for Optical Systems II*, page 254, 1989.

[19] J. L. Pezzaniti and R. A. Chipman. Mueller matrix imaging polarimeter. *Opt. Eng.*, 34(6):1558, 1995.

[20] B. H. Miles, E. R. Cespedes, and R. A. Goodson. Polarization-based active/passive scanning system for minefield detection. *Proc. of SPIE, vol. 1747 Polarization and Remote Sensing*, page 239, 1992.

[21] K. P. Bishop, H. D. McIntire, M. P. Fetrow, and L. McMackin. Multi-spectral polarimeter imaging in the visible to near ir. *Proc. of SPIE, vol. 3699 Targets and Backgrounds: Characterization and Representation V*, page 49, 1999.

[22] H. Takami, H. Shiba, S. Sato, T. Yamashita, and Y. Kobayashi. A near-infrared prism spectrophotopolarimeter. *Publ. Astro. Soc. of the Pacific*, 104:949, 1992.

[23] C. S. L. Chun, D. L. Fleming, W. A. Harvey, E. J. Torok, and F.A. Sadjadi. Synthetic vision using polarization-sensitive, thermal imaging. *Proc. of SPIE, vol. 2736 Enhanced and Synthetic Vision*, page 9, 1996.

[24] R. M. A. Azzam and K. A. Giardina. Photopolarimeter based on planar grating diffraction. *J. Opt. Soc. Am. A*, 10(6):1190, 1993.

[25] R. M. A. Azzam. Diffraction-grating photopolarimeter and spectrophotopolarimeter. *U.S. Patent*, #5,337,146, 1994.

[26] J. R. Maxwell and T. J. Rogne. Advances in polarized infrared imaging, part 1 & 2. *Spectral Reflections, IRIA Newsletter*, 97-01 & 97-04, 1997.

[27] W. A. Shurcliff. *Polarized Light: Production and Use.* Harvard University Press, Cambridge, 1962.

[28] E. Oliva. Wedged double wollaston, a device for single shot polarimetric measurements. *Astron. Astrophys. Suppl. Ser.*, 123:589, 1997.

[29] G. P. Nordin, J. T. Meier, P. C. Deguzman, and M. W. Jones. Micropolarizer array for infrared imaging polarimetry. *J. Opt. Soc. Am. A*, 16(5):1168, 1999.

[30] A. M. Waxman, A. N. Gove, M. C. Seibert, D. A. Fay, J. E. Carrick, J. P. Racamato, E. D. Savoye, B. E. Burke, R. K. Reich, W. H. McGonagle, and D. M. Craig. Progress on color night vision: Visible/ir fusion, perception & search, and

low-light ccd imaging. *Proc. of SPIE, vol. 2736, Enhanced and Synthetic Vision*, page 96, 1996.

[31] H. W. Icenogle, B. C. Platt, and W. L. Wolfe. Refractive indexes and temperature coefficients of germanium and silicon. *Appl. Opt.*, 15:2348, 1976.

[32] N. P. Barnes and M. S. Piltch. Temperature-dependent sellmeier coefficients and nonlinear optics average power limit for germanium. *J. Opt. Soc. Am.*, 69:178, 1979.

[33] R. F. Potter. Optical constants of germanium in spectral region from 0.5ev to 3.0ev. *Phys. Rev.*, 150:562, 1966.

[34] G. Hass and C. D. Salzburg. Optical properties of silicon monoxide in the wavelength region from 0.24 to 14.0 microns. *J. Opt. Soc. Am.*, 44:181, 1954.

[35] A. Thelen. *Design of Optical Interference Coatings.* McGraw-Hill, New York, 1989.

[36] H. A. Macleod. *Thin Film Optical Filters.* McGraw-Hill, New York, 2nd edition, 1989.

[37] J. A. Kong. *Electromagnetic Wave Theory.* John Wiley & Sons, New York, 2nd edition, 1990.

[38] A. Ghatak and K. Thyagarajan. *Optical Electronics.* Cambridge University Press, 1989.

[39] S. Kirkpatrick, C. D. Gelatt Jr., and M. P. Vecchi. Optimization by simulated annealing. *Science*, 220(4598):671, 1983.

[40] F. López and J. de Frutos. Multispectral interference filters and their application to the design of compact non-dispersive infrared gas analyzers for pollution control. *Sensors and Actuators A*, 37:502, 1993.

[41] I. J. Spiro and M. Schlessinger. *Infrared Technology Fundamentals.* Marcel Dekker, New York, 1989.

[42] W. A. Pliskin and H. S. Lehman. Structural evaluation of silicon oxide films. *J. of Electrochem. Soc.*, 112(10):1013, 1965.

[43] E. Ritter. Zur kenntnis der sio- und si2o3- in dünnen schichten. *Opt. Acta*, 9(236):197, 1962.

[44] E. D. Palik, editor. *Handbook of Optical Constants of Solids.* Academic Press, New York, 1985.

[45] F. López and E. Bernabéu. Refractive index of vacuum-evaporated sio thin films: Dependence on substrate temperature. *Thin Solid Films*, 191:13, 1990.

[46] H. H. Li. Refractive index of silicon and germanium and its wavelength and temperature derivatives. *J. Phys. Chem. Ref. Data*, 9:561, 1980.

[47] T. Doumuki and H. Tamada. An aluminum-wire grid polarizer fabricated on a gallium-arsenide photodiode. *Appl. Phys. Lett.*, 71(5):4, 1997.

[48] J. J. Kuta, H. M. van Driel, D. Landheer, and Y. Feng. Coupled-wave analysis of lamellar metal transmission gratings for the visible and the infrared. *J. Opt. Soc. Am. A*, 12(5):1118, 1995.

[49] H. Tamada, T. Doumuki, T. Yamaguchi, and S. Matsumoto. Al wire-grid polarizer using the s-polarization resonance effect at the 0.8-mm-wavelength band. *Opt. Lett.*, 22(6):419, 1997.

[50] Grating Solver Development Co. 2000.

[51] M. G. Moharam and T. K. Gaylord. Diffraction analysis of dielectric surface-relief gratings. *J. Opt. Soc. Am. A*, 72(10):1385, 1982.

[52] M. G. Moharam and T. K. Gaylord. Rigorous coupled-wave analysis of metallic surface-relief gratings. *J. Opt. Soc. Am. A*, 3(11):1780, 1986.

[53] R. Petit, editor. *Electromagnetic Theory of Gratings.* Springer-Verlag, 1980.

[54] Erwin G. Loewen and Evgeny Popov. *Diffraction Gratings and Applications.* Marcel Dekker, 1997.

[55] M. C. Hutley. *Diffraction Gratings.* Academic Press, 1982.

[56] M. C. Hutley, J. F. Verrill, R. C. McPhedran, M. Neviere, and P. Vincent. Presentation and verification of a differential formulation for the diffraction by conducting gratings. *Nouv. Rev. Optique*, 6:87, 1975.

[57] M. A. Jensen and N. P. Nordin. Finite-aperture wire grid polarizers. *J. Opt. Soc. Am. A*, 17(12):2191, 2000.

[58] W. K. Smith. *Modern Optical Engineering; the Design of Optical Systems.* McGraw-Hill, 1966.

[59] J. D. Rancourt. *Optical Thin Films: User Handbook.* SPIE Optical Engineering Press, 1996.

[60] P. K. Chen and C. D. Bass. Efficient wire-grid duplexer polarizer for co2 laser. *Appl. Phys. Lett.*, 18(12):565, 1971.

[61] B.E.A. Saleh and M.C. Teich. *Fundamentals of Photonics.* John Wiley & Sons, Inc., 1991.

[62] J. W. Howard and I. R. Abel. Narcissus: reflections on retroreflections in thermal imaging systems. *Appl. Opt.*, 21(18):3393, 1982.

[63] J. A. Shaw and M. R. Descour. Instrument effects in polarized infrared images. *Opt. Eng.*, 34(5):1396, 1995.

[64] J. H. W. G. den Boer, G. M. W. Kroesen, W. de Zeeuw, and F. J. de Hoog. Improved polarizer in the infrared: two wire-grid polarizers in tandem. *Opt. Lett.*, 20(7):800, 1995.

[65] E. Majkova, S. Luby, M. Jergel, R. Senderak, B. George, M. Vaezzadeh, and J. Ghanbaja. Characterization of obliquely deposited tungsten/silicon multilayers. *Thin Solid Films*, 238:295, 1994.

[66] I. J. Hodgkinson and Q. H. Wu. Practical designs for thin film wave plates. *Opt. Eng.*, 37(9):2630, 1998.

[67] S. S. Wang and R. Magnusson. Multilayer waveguide-grating filters. *Appl. Opt.*, 34(14):2414, 1995.

[68] R. Magnusson and S. S. Wang. Transmission bandpass guided-mode resonance filters. *Appl. Opt.*, 34(35):8106, 1995.